U.PORTO

FEUP FACULDADE DE ENGENHARIA
UNIVERSIDADE DO PORTO

INTEGRATED MASTER IN ENVIRONMENTAL ENGINEERING 2014/2015

Photocatalytic Reduction of CO_2 into Renewable Fuels

João Ricardo Gomes Vaz Silva

Dissertation for the Degree of:

MASTER IN ENVIRONMENTAL ENGINEERING

Developed at:

Laboratory of Catalysis and Materials (LCM)

President of the Jury:

Supervisor: Adrián M.T. Silva (Principal Investigator)

Co-supervisor: Luisa M. Pastrana-Martínez (Auxiliary Investigator)

Co-supervisor: Joaquim L. Faria (Associate Professor)

Department of Chemical Engineering
Faculty of Engineering - University of Porto

Porto, July 2015

Agradecimentos

Aproveito esta pequena seção para expressar a minha profunda e sincera gratidão a todos aqueles que direta e indiretamente contribuíram para a realização desta dissertação, inserida no Mestrado Integrado em Engenharia do Ambiente e desenvolvida no Laboratório de Catálise e Materiais da Faculdade de Engenharia da Universidade do Porto.

Aos meus caríssimos orientadores, Doutor Adrián Silva, Doutora Luísa Pastrana-Martinez e Professor Doutor Joaquim Faria, pelos vastos conhecimentos transmitidos, sugestões, simpatia e disponibilidade total. Muito obrigado por tudo.

Ao Professor Doutor José Luís Figueiredo, Diretor do Laboratório de Catálise e Materiais (LCM) por ter disponibilizado todos os recursos necessários à execução deste trabalho. Ao Dr. Carlos Sá do CEMUP (Centro Materiais da Universidade do Porto) pela assistência com as análises de microscopia eletrónica de varrimento (SEM).

Agradeço aos colegas investigadores do LCM, pela forma como me receberam, pela amizade, pelas preciosas dicas e bons momentos.

Aos meus Pais, por terem financiado este dispendioso percurso de 5 anos que agora termina, pelo constante apoio, pela curiosidade e também pelo orgulho que sempre tiveram em mim.

A três outros familiares muito especiais, nomeadamente, à minha avó Beatriz Chilro, à minha tia Fátima Vaz e em especial ao meu irmão Pedro Vaz.

A minha melhor amiga e namorada Marta Barbosa, por ser simplesmente a pessoa mais importante, uma grande conselheira, um exemplo de trabalho e sobretudo de superação. Obrigado também por todas as horas que passámos juntos em prol deste longo e trabalhoso curso.

Por último, queria dedicar inteiramente esta dissertação ao meu grande amigo e companheiro de equipa, Marlon Jacinto Barbosa Correia. Fui um grande privilegiado por ter tido a tua amizade e ter conhecido essa forma de estar numa vida que tão barbaramente te foi arrancada. Até Sempre Amigo.

Abstract

In recent decades, rising atmospheric levels of carbon dioxide (CO_2) and exhaustion of fossil fuel reserves raised considerable public concern. Photocatalytic conversion of CO_2 to valuable chemicals (such as methanol) using solar energy has attracted considerable attention due to the great potential to provide an alternative clean fuel and solve the problems related to the global warming.

This dissertation presents a literature survey on the photocatalytic reduction of CO_2 for the production of solar fuels, including the synthesis of active carbon-based photocatalysts for this application, together with several other strategies that have been implemented to enhance the photocatalytic efficiency of CO_2 reduction. In particular, it is discussed the role of carbon nanotubes (CNT), graphene and graphitic carbon nitride (g-C_3N_4) based materials, in critical issues such as extending the light absorption to visible range of the electromagnetic spectrum, increasing the separation of charge carriers, the band gap engineering and preferential adsorption of CO_2.

This work also shows experimental results on the aqueous phase photocatalytic reduction of CO2, to methanol and ethanol (renewable fuels), under UV-Vis light irradiation. Composites of graphene-oxide/titanium-dioxide (GOT) were prepared by the liquid phase deposition method and tested in this reaction. The addition of metallic platinum and copper as co-catalysts over the commercial TiO_2 Degussa P25 material (1 wt. % Pt-Cu/P25) was also investigated. These photocatalysts were characterized by different techniques, including N_2 adsorption, temperature programmed reduction (TPR), scanning electron microscopy (SEM), attenuated total reflection Fourier transform infrared (ATR-FTIR) and diffuse reflectance UV-Vis spectroscopy (DRUV). In addition, the effect of initial pH on the photocatalytic CO_2 reduction was investigated.

It is found that the 1 wt. % Pt-Cu/P25 photocatalyst increased both methanol and ethanol formation rates at initial pH 13, relatively to bare P25, probably due to suppression of surface electron/hole recombination by the bimetallic phase of the co-catalyst. The GOT composite yielded the highest photocatalytic activity (for ethanol formation at pH 13 and for methanol formation at pH 3), which can be justified by the improved adsorption of reactants and efficient interfacial electron transfer between the two constituent phases.

Keywords: Climate change; CO_2 photoreduction; Solar fuels; Photocatalysts; TiO_2; Graphene oxide; Copper; Platinum.

Resumo

Nas últimas décadas, o aumento dos níveis atmosféricos de dióxido de carbono (CO_2) e o esgotamento das reservas de combustíveis fósseis têm suscitado grande preocupação pública. O interesse pela conversão fotocatalítica de CO_2 em produtos de valor acrescentado, tais como o metanol, tem aumentado significativamente por parte da comunidade científica, principalmente quando utilizada energia solar para este efeito. O potencial de produzir e fornecer um combustível limpo, minimizando simultaneamente os problemas relacionados com o aquecimento global, são os principais motivos associados a este interesse.

A presente dissertação inclui um trabalho de revisão bibliográfica sobre os mais recentes avanços na síntese de fotocatalisadores derivados de materiais de carbono e respetiva aplicação na redução fotocatalítica de CO_2 para produzir combustíveis solares. Em particular, é discutido o papel dos nanotubos de carbono, dos materiais de grafeno e de nitretos de carbono grafítico, em aspetos importantes como a expansão da gama de absorção para o espectro visível, separação das vias de transporte de cargas, estruturação de bandas de condução e valência do semicondutor e ainda a adsorção preferencial de CO_2.

Neste trabalho são também apresentados resultados experimentais obtidos para a redução fotocatalítica do CO_2, em fase aquosa, com vista à produção de metanol e etanol sob irradiação no ultravioleta-visível. Para este efeito, foram preparados materiais compósitos de óxido-de-grafeno/dióxido-de-titânio (GOT) pelo método de deposição em fase líquida. A introdução de platina e cobre como co-catalisadores sobre o material comercial de TiO_2 Degussa P25 (1 % de Pt-Cu/P25) foi também estudada. A caracterização destes materiais foi realizada pelas técnicas de adsorção de N_2, redução a temperatura programada (TPR), microscopia eletrónica de varrimento (SEM), espectroscopia por transformada de Fourier com reflexão total atenuada (ATR-FTIR) e refletância difusa de UV-Visível (DRUV). Foi ainda estudada a influência do pH inicial na reação de redução fotocatalítica de CO_2.

A atividade catalítica para a formação de etanol e metanol (pH inicial de 13) na presença do fotocatalisador 1 p/p % Pt-Cu/P25, é muito superior à obtida com o P25, provavelmente devido à supressão do processo de recombinação electrão/buraco. O compósito GOT apresentou a maior atividade fotocatalítica para formação de etanol (a pH 13) e metanol (a pH 3), a qual pode ser justificada por uma melhor adsorção dos reagentes e um processo mais eficaz de transferência eletrónica na interface dos materiais que constituem o catalisador.

Palavras-chave: Alterações climáticas; Fotoredução do CO_2; Combustíveis solares; Fotocatálise; TiO_2; Óxido de grafeno; Cobre e platina.

Nomenclature

ATR-FTIR	Attenuated Total Reduction Fourier Transformed Infrared
CB	Conduction Band
CCS	Carbon Capture and Storage
CNT	Carbon Nanotubes
DRUV	Diffuse Reflectance Ultraviolet-Visible Spectroscopy
Eg	Bandgap Energy
EDS	Energy-dispersive X-ray spectroscopy
FID	Flame Ionization Detector
GC	Gas Chromatography
GE	Greenhouse Effect
GO	Graphene Oxide
GHG	Greenhouse Gas
GWP	Global Warming Potential
IUPAC	International Unit of Pure and Applied Chemistry
LED	Light Emitting Diode
MCN	Melamine Carbon Nitride
MEA	Monoethanolamine
MMT	Montmorillonite
PZC	Point of Zero Charge
PV	Photovoltaic
S_{BET}	Specific Surface Area by Brunauer–Emmett–Teller method
SEM	Scanning Electron Microscopy
SROWE	Statistical Review of World Energy

TCD	Thermal Conductivity Detector
TCN	Thiourea Carbon Nitride
TPR	Temperature Programmed Reduction
VB	Valence Band
XPS	X-ray Photoelectron Spectroscopy

Table of Contents

Agradecimentos i
Abstract ii
Resumo iii
Nomenclature iv
1. Introduction 1
1.1 How Climate Change Drives Solar Fuel Development 1
1.1.1 Climate change 1
1.1.2 Fossil Fuel Exhaustion and Solar Energy Storage 4
1.2 Converting CO_2 into Solar Fuels 6
1.3 Objectives 7
1.4 Presentation of the Research Unit 8
1.5 Structure of the Dissertation 9
2 Solar Fuels: a State of the Art 10
2.1 Photocatalytic Reduction of CO_2 into Fuels 10
2.1.1 Basic Principles 10
2.2 Carbon-Based Photocatalysts 12
2.2.1 Carbon Nanotubes (CNTs) Based Photocatalysts 13
2.2.2 Graphene-Based Photocatalysts 16
2.2.3 Graphitic Carbon Nitride-Based Photocatalysts 20
2.3 Water as Reducing Agent 25
2.4 Other Electron Donors 28
3 Experimental Section 31
3.1 Chemicals 31
3.2 Synthesis of Graphene Oxide 31
3.3 Preparation of Graphene Oxide-TiO_2 Composite 32
3.4 Preparation of Bimetallic Loaded Catalysts 32
3.5 Catalyst Characterization 33
3.6 Photocatalytic CO_2 Reduction Experiments 34
4 Results and Discussion 37
4.1 Photocatalysts Characterization 37
4.1.1 N_2 Adsorption–Desorption Isotherms 37
4.1.2 Temperature Programmed Reduction 38
4.1.3 Scanning Electron Microscopy 38

4.1.4 Attenuated Total Reflection Fourier Transform Infrared 39
4.1.5 Diffuse Reflectance UV-Vis Spectra 40
4.2 Photocatalytic Reduction of CO_2 41
5 Conclusions 46
6 Future Work 48
References 49
Appendix A: Calibration Curves 57

List of Tables

Table 1 - Pre-1750 and recent tropospheric concentration, atmospheric lifetime and GWP of greenhouse gases. 3
Table 2 - Two, four, six, eight and twelve electron reduction potentials (vs NHE) of some reactions involved in CO_2 photoreduction 12
Table 3 - Recent works on photocatalytic reduction of CO_2 over CNT-based photocatalysts 14
Table 4 - Recent work on photocatalytic reduction of CO_2 over graphene-based photocatalysts 18
Table 5 - Recent work on photocatalytic reduction of CO_2 over graphitic carbon nitride-based photocatalysts 21
Table 6 – Examples of electron donors applied in liquid or gaseous phase. 29
Table 7 – Reagents employed in the catalysts preparation and CO_2 reduction experiments. 31
Table 8 – Composition of the solutions used in the photocatalytic reactions. 35
Table 9 – BET surface area (SBET), relative amount of anatase and rutile crystalline phases and the band-gap energy (Ebg) of catalysts 37

List of Figures

Figure 1 - a) Natural greenhouse effect and b) human enhanced greenhouse effect. 2
Figure 2 – Evolution of atmospheric CO_2 concentration during the last 800,000 years. 3
Figure 3 - Total world energy consumption by source in 2013. 5
Figure 4 - Mechanism of CO_2 photocatalytic reduction on TiO_2 semiconductor. 10
Figure 5 – Energy correlation between semiconductors catalysts and redox couples. 11
Figure 6 - Photoexcitation of the MWCNT/TiO_2 nanocomposites and the subsequent electron charge transfer. 15
Figure 7 - Yield of photocatalytic products of Ag@AgBr and Ag@AgBr/CNT nanocomposites with different CNTs lengths. 16
Figure 8- Energy band positions of rGO, Pt, Pd, Ag and Au, including the conduction and valence bands of TiO_2 photocatalyst. 19
Figure 9 - UV–vis spectra of ZnO-RGO nanocomposites and ZnO particles. 20

Figure 10 – Photoluminescence spectra of ZnO and ZnO-rGO composites with excitation wavelength of 325 nm. 20
Figure 11- Schematic of the generation of CH_4 and CH_3CHO on bulk g-C_3N_4 and g-C_3N_4 nanosheets in the photoreduction of CO_2 in the presence of water vapor. 23
Figure 12 – Influence of the platinum content on the photocatalytic performance of g-C_3N_4. 24
Figure 13 – Transient photocurrent responses of TCN and MCN. 25
Figure 14 – Distribution of carbonate species as a fraction of total dissolved carbonate in relation to solution pH. 26
Figure 15 - Photocatalytic reduction of CO_2 at different pH, using a graphene-TiO_2 composite. 27
Figure 16 - Influence of the initial pH level in the photocatalytic reduction of CO_2, using $AgBr/TiO_2$. 27
Figure 17 - The influence of Na_2SO_3 concentration on the product yield. 29
Figure 18 – Schematic representation of the procedure used for preparation of bimetallic catalysts (Pt-Cu/P25 and Pt-Cu/GOT). 33
Figure 19 – Photocatalytic reaction setup. 34
Figure 20 – Irradiance spectra of the Heraeus TQ-150 UV-Vis lamp equipped with a DURAN 50 ® jacket and transmittance spectrum of the cut-off filter. 35
Figure 21 – N_2 adsorption–desorption isotherms at −196 ºC for Pt-Cu/P25 and for the Pt-Cu/ GOT composites. 37
Figure 22 - TPR profiles of the Pt-Cu/P25 catalyst. 38
Figure 23 – SEM images of GOT (a), P25 (b), Pt-Cu/GOT (c,d) and Pt-Cu/P25 (e). SEM images recorded with backscattered electrons detection of Pt-Cu/GOT (d) EDS spectrum of Pt-Cu/P25 (f). 39
Figure 24- ATR spectra of GO, P25, GOT and the Pt-Cu loaded catalysts. 40
Figure 25- DRUV-Vis spectra of P25, GOT and Pt-Cu/P25 catalysts. 41
Figure 26- Photocatalytic reduction of CO_2 at different initial pH for a) P25 and b) GOT. 42
Figure 27- CO_2 photoreduction over P25 and Pt-Cu/P25 at initial pH 13. 44
Figure 28 – Methanol Calibration Curve 57
Figure 29 – Ethanol Calibration Curve 57

1. Introduction

1.1 How Climate Change Drives Solar Fuel Development

1.1.1 Climate change

Climate change is one of the primary concerns for humanity in the 21st century [1]. Earth's average surface temperature unusually has risen by 0.6-0.9 ºC since 1906, and the rate of temperature increase approximately doubled in the last 55 years [2]. The scientific community has spent decades evaluating the causes of sudden global warming. Natural cycles and specific events, like slight wobbles in the planet orbit, volcanic eruptions or even variations in the solar brightness, are known to have some climate influences. However, the amount and pattern of warming cannot be solely explained by natural causes, and the concept of anthropogenic greenhouse gases (GHGs) surged. In order to understand how GHGs severely influence the climate, the concept of greenhouse effect (GE) must be firstly discussed.

The solar constant is the amount of energy that perpendicularly strikes on a unit area of the earth's atmosphere, per second, when the planet is at its mean distance from the sun. The value of the constant is approximately 1366 W m^{-2} [3]. Approximately, one third of the extraterrestrial solar radiation is reflected directly back into space by reflective surfaces like clouds, ice, and sand. The remaining two thirds is absorbed by the land, oceans and, to a lesser extent, by the atmosphere. As the rocks, the air, and the seas heat up, they radiate the same amount of energy back to space, to balance the absorbed incoming energy, at much longer wavelengths, mainly in the infrared part of the spectrum, according to Planck's Law. Much of this thermal radiation emitted by the land and ocean is absorbed by water vapor and greenhouse gases molecules present in the atmosphere. Following the same physical principle, microscopic water or greenhouse gas molecules re-emit most of the energy that radiates upward from the Earth's surface, adding the heat back to the lower atmosphere and maintaining Earth's average surface temperature at 15 ºC (**Figure 1a**). Since the Industrial Revolution, man-made activities have added significant quantities of GHGs to the atmosphere, mostly from the combustion of coal, oil and other fossil fuels. The emissions of these GHGs have been accepted as the main source of global warming (**Figure 1b**).

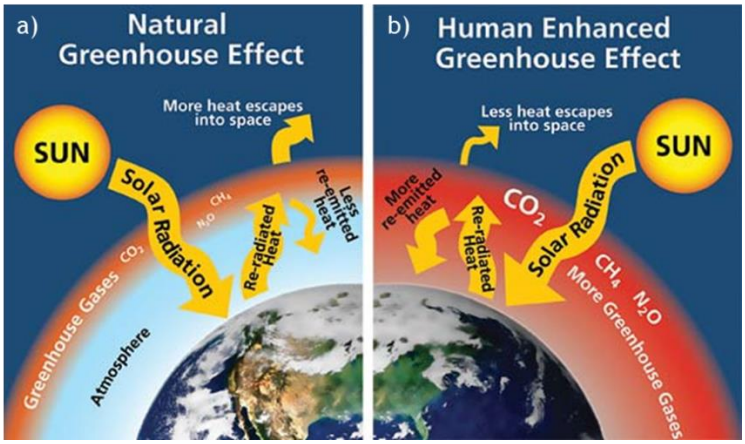

Figure 1 - a) Natural greenhouse effect and b) human enhanced greenhouse effect. Reprinted from Ref. [4].

The most abundant GHG in Earth's atmosphere is water vapor; others like carbon dioxide, methane, nitrous oxide, and to a lesser extent ozone and chlorofluorocarbons also contribute to the observed phenomena. Some gases are more critical than others. In order to quantitatively compare the GE of different gases, a global warming potential (GWP) index has been used which is based on the ratio of the radioactive forcing of an equal emission of two different gases, integrated either overall time or up to an arbitrarily determined time horizon. GWP is expressed as a factor of CO_2 (whose GWP is standardized to 1).

The past and recent tropospheric concentrations, atmospheric lifetime and GWP of several GHGs is shown in **Table 1**. Water vapor was not included, considering that the atmospheric concentration of this potent GHG is highly influenced by the air temperature. Thus, it is difficult to determine its concentration. CO_2 plays a very important role in the greenhouse effect, due to its abundance and longevity in the atmosphere.

Table 1 - Pre-1750 and recent tropospheric concentration, atmospheric lifetime and GWP of greenhouse gases. Adapted from Ref. [5].

Gas	Pre-1750 concentration	Recent concentration	Atmospheric lifetime (years)	GWP
Concentrations in parts per million				
Carbon Dioxide (CO_2)	280	404	~100-300	1
Concentrations in nanomol.mol^{-1}				
Methane (CH_4)	722	1762-1893	12	28
Nitrous Oxide (N_2O)	270	324-326	121	265
Tropospheric Ozone (O_3)	237	337	Hours-days	n.a
Concentrations in picomol.mol^{-1}				
Sulfur Hexafluoride (SF_6)	0	8	3200	23 500
CFC-12 (CCl_2F_2)	0	527	100	10 200
Halon 1301 ($CBrClF_3$)	0	3	65	6 290

The concentration of CO_2 increased at a rate of ca. 1 % per year, but this increment per year has shifted to > 2 % over the last 25 years [6]. Scientific studies reveal that the CO_2 concentration has increased from 280 ppm in the preindustrial era to 404 ppm in 2015 (**Figure 2**). According to the accepted models, current CO_2 concentration far exceeds its natural fluctuation over the past 800 000 years.

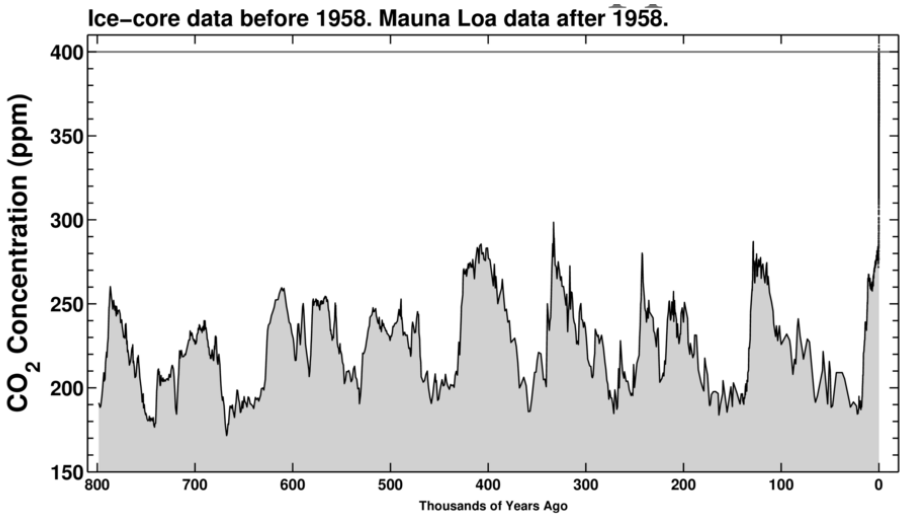

Figure 2 - Evolution of atmospheric CO_2 concentration during the last 800,000 years. Reprinted from Ref. [7].

Global CO_2 emissions reached a new maximum of 35300 million tonnes in 2013, which represents an increase of 2 % compared to 2012 [8]. Energy intensive activities using fossil fuels and cement production were of the highest relevance, accounting for 90 % of total emissions. Among fossil fuels, coal consumption was responsible for about 44 % of emissions [8]. If CO_2 releasing trends persist, then the global temperature would be greater than 4.5 ºC by 2050 [9], resulting in severe impacts as rising of sea level, endangerment and even extinction of plants and animals, human health effects, floods, droughts and even an economic collapse can be predicted.

Great effort has been made to reduce CO_2 emissions. The amount of technologies involving carbon capture and storage (CCS) has increased during the past decade. However, CCS has a number of economic and technical limitations such as large capital investment, CO_2 leakage rates uncertainty, and unavailability of storage locations, in this way increasing CO_2 transportation and injection costs [10]. Moreover, since CCS requires high energy inputs, the consequence is a larger carbon footprint and does not alleviate significantly the society from the dependence on diminishing fossil fuels.

1.1.2 Fossil Fuel Exhaustion and Solar Energy Storage

Another important challenge faced nowadays is the development of technologies based on renewable energy resources, able to support current and future global energy demands. Energy is inherently coupled to the development and better quality of life. Its needs are growing, due to current lifestyles based on consumerism, demographic growth and economic development of newly industrialized countries. Currently, world annual energy consumption is ca. 17 terawatt (TW) and it is expected to be ca. 26 TW by 2040 [11, 12].

British Petroleum annually publishes a Statistical Review of World Energy (SROWE). It is seen as one of the most reputed and utilized publications in energy economics, valued by governments, academics, and professionals worldwide. The statistics included in this review

are provided by government and other primary sources. Global primary energy consumption information can be accessed in SROWE 2014, among other relevant information (**Figure 3).**

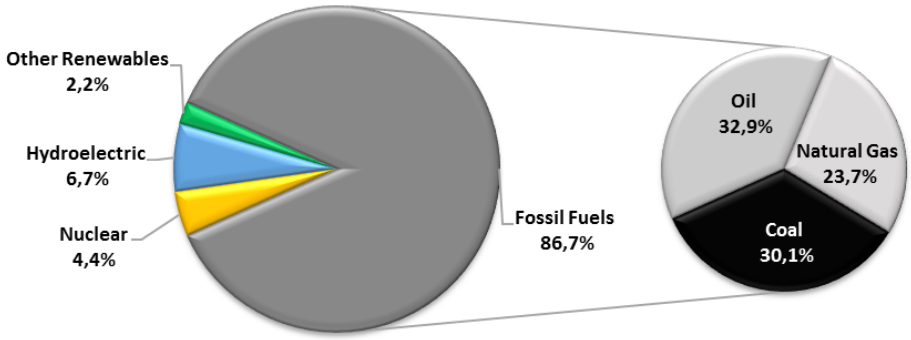

Figure 3 - Total world energy consumption by source in 2013. Adapted from [12]

Fossil fuels accounted for about 86.7 % of the world's primary energy consumption in 2013. Within this category, oil remained the prime fuel with 32.9 % of market share, while coal and natural gas had respectively 30.1 and 23.7 %. Fossil fuels continue leading the energy market, once they can provide unfailing power from relatively small areas, at affordable prices and principally in the enormous quantities required. Nevertheless, fossil fuels are non-renewable energy resources and their reserves are being depleted much faster than replenished. If 2013 trends of energy consumption persist, proven reserves of crude oil and coal will be exhausted within 51 and 111 years, while the last cubic meter of natural gas will be extracted in 2069 [12].

A global movement towards the generation of renewable and green sources of fuels and electricity is under way. In 2013, 4.4 % of the energy necessities were met by nuclear energy, whereas hydroelectric and other renewables as solar, tidal, geothermal, wind and biomass accounted for 6.7 and 2.2 %, respectively [12].

However, the energy supplied by nuclear technologies is unable to provide liquid fuels necessary for transportation. In addition, this technology is unsafe, as demonstrated by the nuclear power plant disaster in Japan due to earthquake and tsunami in March 2011 [13]. Although, in the medium to long term, prospects for nuclear energy remain positive for China, India, Middle East Countries and Russia, the hypothesis of nuclear power replacing fossil fuels worldwide is weak.

Utilization of biomass offers possibilities for the implementation of the waste to wealth concept by converting forest, agriculture and municipal solid wastes into 5-7 TW of bioenergy or biofuels. Other renewable sources like wind, hydroelectric, geothermal and tides, can provide ca. 2.1, 1.5, 5 TW and ca. 2 TW, respectively [9, 14-16].

In contrast, the amount of sunlight striking the earth's atmosphere continuously is 1.75 x 10^5 TW. Considering a 60 % transmittance through the atmospheric cloud cover, 1.05 x 10^5 TW reaches the earth's surface continuously [17]. In other words, converting about 10 % of the solar energy on 0.3 % of the Earth's surface would be enough to largely exceed the projected energy needs in 2040 [18]. Even so, solar-generated energy, at the moment, does not compete successfully with that from fossil fuels. The diurnal nature of solar radiation, the fluctuation of sunlight intensity at the earth's surface as a function of the season and weather conditions, and the diffuse nature of solar energy require proper storage methods [19]. The majority of solar energy storage techniques developed so far possess low energy densities. For example, compressed air at 300 bar, batteries, flywheels, supercapacitors, and pumped storage hydroelectricity are estimated to accumulate ~0.5, ~0.1–0.5, ~0.5, ~0.01, and ~0.001 MJ/kg, respectively [20]. Therefore, solar energy storage is still in its infancy stage and great progresses are urgently needed in order to harness the power of the Sun and replace exhaustible and dirty fossil fuels.

1.2 Converting CO_2 into Solar Fuels

Recycling of easy available and renewable carbon resources, as CO_2, into a high-energy content fuel, compatible with the existing hydrocarbon based energy infrastructures, would be a fascinating solution towards sustainability. Though, the biggest difficulty to the development of this strategy is the low energy level of the CO_2 molecule. It is thermodynamically stable and high inputs of energy are required for breaking the double bond (C=O) and transform it into useful fuels [21]. Energy requirements must be introduced with renewable energy sources to reduce the carbon and environmental footprint, and considering the properties of solar energy, there is much current interest in developing fuels obtained from sunlight. Hence, transformation of CO_2 into Solar Fuels would mitigate global warming, soften fossil fuel depletion and provide high-density solar energy storage via chemical bonds.

The concept of Solar Fuels refers mainly to the generation of hydrogen from water and products derived from CO_2 such as methanol, methane, formic acid and other chemicals. Hydrogen can be produced from water using renewable solar energy, through a wide range of processes, namely, electrolysis, photo-electrochemical, photo-catalytic and thermochemical water splitting [22-24]. Herron et al. [23] reviewed the solar fuel technologies and concluded that water electrolysis coupled with photovoltaic (PV) technology is a near-term and reasonable efficient solution to produce clean hydrogen. On

the other hand, photo-electrochemical and thermochemical water splitting technologies are more complex to design, but they obtain similar solar-to-hydrogen efficiencies [23]. However, there are currently numerous problems and limitations associated with the use of hydrogen, i.e. the problems associated to the storage of reasonable volumes of this gas under ambient conditions, as well as problems derived from the risk due to flammability and explosion.

The implementation of Solar Fuels derived from CO_2, and particularly methanol, offers more advantages because this product: (i) is more valuable as transportation fuel, due to the high energy content; (ii) is a liquid compound with a relatively high boiling point; and (iii) can be combined as an additive of fossil fuels used in standard automotive engines. Besides methanol, the second most interesting solar fuel resulting from CO_2 reduction would be methane. The main advantage of methane is that this compound is consumed in massive quantities in the industry. So, if obtained from CO_2 and a renewable energy resource, its use will be sustainable and even neutral from the point of view of CO_2 footprint.

CO_2 conversion can be attained through its reaction with hydrogen (by Reverse Water Gas Shift) producing syngas or through reaction of carbon monoxide (obtained by solar conversion of CO_2) with hydrogen [15, 23, 25]. CO_2 may also be directly transformed to fuels using solar energy through PV-electro-catalytic, photo-electrochemical, photo-catalytic and thermochemical reduction. In comparison with catalytic conversion using hydrogen, CO_2 direct reduction is much simpler. Nonetheless, these novel processes have been much less developed and remain less efficient [23]. Among all the mentioned strategies, the direct use of sunlight to reduce CO_2 by water, in the presence of a photocatalyst, is an ideal solution to the global warming and energy problems. However, this process is also very far from a mature stage.

1.3 Objectives

As referred above, the photocatalytic reduction of CO_2 is seen as an ideal future strategy to reduce the atmospheric concentration of CO_2 and produce value added fuels through a highly sustainable way. The scientific community has been doing great efforts in this way, trying to increase the yields of diverse products resulting from CO_2 reduction reactions. To achieve this goal, it is urgent the development of highly active/stable photocatalysts, as well as to study the influence of the reaction conditions and unravel the underlying reduction mechanisms.

This dissertation has been divided in two parts:

In the first one, an overview of the general aspects of the photocatalytic reduction of CO_2 into solar fuels will be given and the roles of key parameters such as reduction potentials, water as reducing agent and the employment of others electron donors have been discussed in detail, considering the published literature.

The second part of this thesis is dedicated to the development of different photocatalysts and to study their performance in CO_2 photoreduction. In this experimental part, the following specific objectives were defined:

- Synthesis of graphene oxide-TiO_2 (GOT) composites;
- Preparation of bimetallic (copper and platinum) loaded TiO_2 and GOT catalysts;
- Characterization of the prepared materials using different techniques;
- Evaluate the effects of bimetal deposition and/or graphene oxide coupling in the performance of TiO_2, as well as the effect of the initial pH on the photocatalytic reduction experiments.

1.4 Presentation of the Research Unit

The Laboratory of Catalysis and Materials (LCM), in partnership with the Laboratory of Separation and Reaction Engineering (LSRE), became a national Associate Laboratory in 2004, in recognition of the capacity of the two units to cooperate in a stable, competent and effective way in the prosecution of specific objectives of the National Scientific and Technological Policy. The Associate Laboratory is located in the Chemical Engineering Department of the Faculty of Engineering of University of Porto (FEUP), with two external Poles at Instituto Politécnico de Bragança and Instituto Politécnico de Leiria. FEUP is a public institution of higher education with financial autonomy and the largest Faculty of the University of Porto.

The present work is in line with the objectives of the Research line on Catalysis and Carbon Materials, specifically in what concerns the group works on Photochemistry and Photocatalysis leading to the development of new catalytic technologies for efficient energy production and synthesis of high performance carbon-semiconductor photocatalysts for solar fuels production. The work was carried out at the associate laboratory LSRE-LCM located in the Department of Chemical Engineering/FEUP (E-301, E-302A and E-303). A lab-scale set-up for the photocatalytic reduction of CO_2 equipped with a Heraeus TQ 150 medium pressure

mercury vapor lamp, which was built and optimized in the framework of this MSc Dissertation, was used together with a gas chromatograph, using a flame ionization detector (FID) and a thermal conductor detector (TCD). Different equipment for the characterization of the prepared photocatalysts were also employed in this dissertation.

1.5 Structure of the Dissertation

The dissertation is organized into 5 chapters:

(i) The first chapter describes the global problem that is under investigation in this work, the respective objectives of this Thesis as well as presents the Research Unit.

(ii) The second chapter describes the state of the art in this topic by performing an overview of the literature.

(iii) The third chapter describes the procedures employed to prepare the photocatalysts, details the materials characterization methodologies and the conditions of the photocatalytic reduction experiments.

(iv) The fourth chapter consist of the results obtained from the characterization of the prepared materials and the respective photocatalytic runs.

(v) The fifth chapter includes the overall conclusions and future work to be developed.

2 Solar Fuels: a State of the Art

2.1 Photocatalytic Reduction of CO_2 into Fuels

2.1.1 Basic Principles

Photocatalytic reduction of CO_2 takes advantage of a photo sensitive semiconductor material to promote a set of reactions in the presence of light. The development of effective semiconductor photocatalysts has therefore emerged as one of the most important goals in materials science. Some of the most adequate and traditionally studied semiconductors are TiO_2, ZnO, CdS, ZnS, Fe_2O_3 and WO_3 [26]. When a semiconductor is illuminated with photons of energy *hv* that is equal to or higher than its band-gap E_G ($hv \geq E_G$), these photons are absorbed and create high energy electron-hole pairs, which dissociate into free photoelectrons in the conduction band and photoholes in the valence band [27]. The photo-generated electrons and holes that migrate to the surface of the semiconductor without suffering recombination can, respectively, reduce carbon dioxide and oxidize a reductant, both adsorbed on the semiconductor surface. The lifetime of an excited electron–hole pair is limited to a few nanoseconds, but this time is enough to promote redox reactions in the solution or in the gas phase when they are in contact with the semiconductor [28]. **Figure 4** depicts a representation of the CO_2 photocatalytic reduction mechanism.

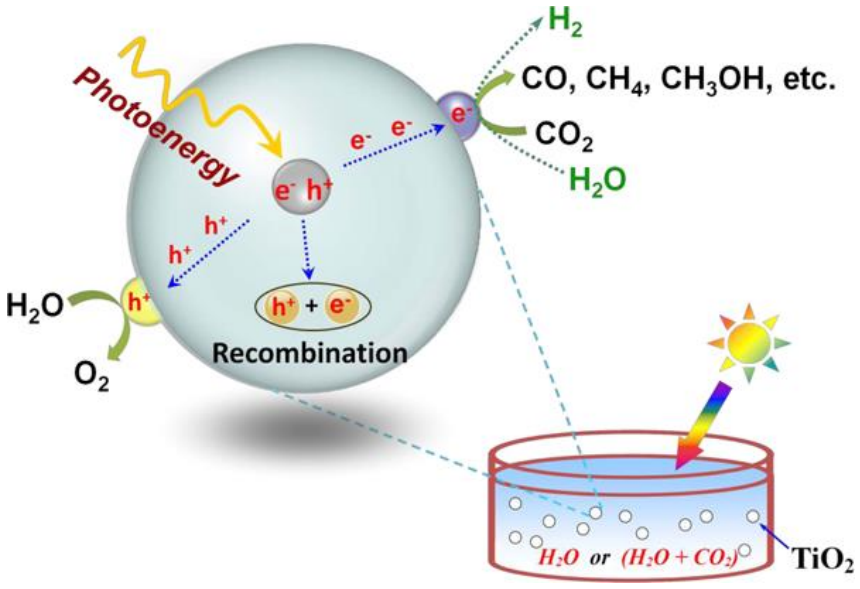

Figure 4 - Mechanism of CO_2 photocatalytic reduction on TiO_2 semiconductor. Reproduced with permission from Ref. [29]. Copyright (2014), American Chemical Society.

CO_2 is one of the most stable and inert compounds of carbon and its conversion into hydrocarbon fuels is highly unfavorable, considering thermodynamic and kinetic drawbacks. The single-electron reduction of CO_2 to an anion radical $CO_2^{\cdot-}$ has a strong reduction potential of -1.9 V *vs* the normal hydrogen electrode, due to a large reorganizational energy between the linear molecule of CO_2 and bent radical anion [18, 30]. Thus, none of the semiconductors involved in CO_2 reduction is able to provide sufficient potential to transfer a single photogenerated electron to a free CO_2 molecule (**Figure 5**).

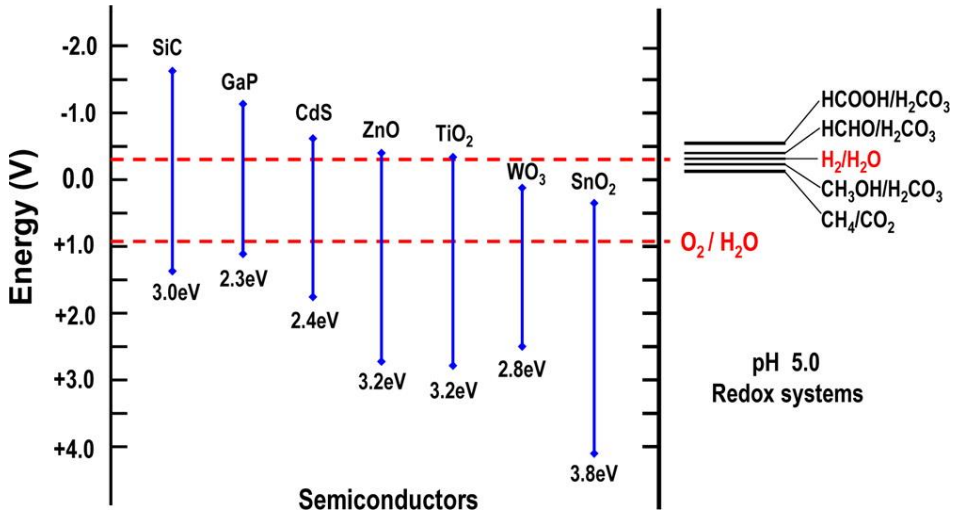

Figure 5 - Energy correlation between semiconductors catalysts and redox couples. Reprinted with permission from Ref. [29]. Copyright (2014), American Chemical Society.

The proton coupled multi electron steps are thermodynamically favored over the single-electron transfer transformation, as shown in **Table 2** [31, 32].

Table 2 - Two, four, six, eight and twelve electron reduction potentials (vs NHE) of some reactions involved in CO_2 photoreduction [18, 33] **.**

Reaction	E°_r (V) vs NHE [(a)]
(1) $CO_2 + 2H^+ + 2e^- \rightarrow HCOOH$	-0.61
(2) $CO_2 + 2H^+ + 2e^- \rightarrow CO + H_2O$	-0.53
(3) $CO_2 + 4H^+ + 4e^- \rightarrow HCHO + H_2O$	-0.48
(4) $CO_2 + 6H^+ + 6e^- \rightarrow CH_3OH + H_2O$	-0.38
(5) $CO_2 + 8H^+ + 8e^- \rightarrow CH_4 + 2H_2O$	-0.24
(6) $2CO_2 + 12H^+ + 12e^- \rightarrow C_2H_5OH + 3H_2O$	-0.16
(7) $2H^+ + 2e^- \rightarrow H_2$	-0.41

(a) E°_r reported at pH 7 and unit activity

These multiple-electron pathways require less energy per electron transfer, compared to single-electron reduction, increasing the feasibility of the process. Importantly, the potential of the acceptor is lower (more positive), than the conduction band of the semiconductors depicted in **Figure 5** [18, 34].

A great variety of final products may be obtained, determined by the specific reaction pathway and the number of electrons and protons involved in the chemical reactions. The products category might include carbon monoxide, organic compounds including formic acid (HCOOH), formaldehyde (HCHO), methanol (CH_3OH), methane (CH_4) as well as higher molecular weight hydrocarbons. The formation of desirable fuels, such as CH_3OH and CH_4, is a thermodynamically facile process, as it occurs at lower reduction potentials, relatively to other products. Nevertheless, CH_3OH and CH_4 evolution is kinetically less favorable, since six and eight electrons, as well as corresponding protons, are respectively involved in their generation (**Table 2**).

2.2 Carbon-Based Photocatalysts

The solar photocatalytic reduction of CO_2 has the potential of being a way of recycling CO_2 and of storing intermittent solar energy in synthetic carbon neutral fuels. To achieve this goal, there is an imperative necessity to develop photocatalysts meeting the following conditions: (i) small band gap so that a large part of the visible light spectrum can be

absorbed [18]; (ii) efficient separation and migration of the photo-generated charge carriers; and (iii) enough quality and quantity of active sites should be provided, such as adsorption sites and reaction centers, contributing to the photocatalytic reaction [21].

A pioneering study was reported in 1979, when Inoue et al. [35] demonstrated the photocatalytic reduction of CO_2 into small amounts of organic compounds, such as formaldehyde, methyl alcohol and methane. The semiconductor photocatalysts tested were TiO_2, ZnO, CdS, GaP, SiC and WO_3, suspended in CO_2 saturated water, under ultraviolet irradiation. This work encouraged many studies and several other semiconductors have been explored. Among all the semiconductor materials, TiO_2 and TiO_2-based heterogeneous photocatalysts have been studied more extensively, due to their low-cost and high chemical stability. However, other photocatalytic systems have also been deeply investigated, involving sulfides, nitrides and phosphides, among others.

In spite of having started 36 years ago, CO_2 photocatalytic conversion state-of-the art is far away from implementation in large-scale, and still considered a utopia. The highest efficiencies commonly do not exceed tens of μmol of product per hour of illumination per gram of photocatalyst. Several studies have shown that the catalytic efficiency is mainly compromised by the low visible-light absorption of the photocatalyst and by the high electron−hole recombination rates in the semiconductor material. In order to overcome this situation, several approaches have been employed. In 2014, Tu et al. [21] published an overview of the state-of-the-art accomplishments in the design and engineering of photocatalysts, involving bandgap engineering, nanostructuration, surface oxygen vacancy engineering, textural control, exposure of highly active crystal facets and Z-scheme construction, and employment of co-catalysts.
According to the literature, a great deal of recent attention has been devoted on the combination of semiconductors with carbonaceous materials, including carbon nanotubes, graphene and its derivatives and graphitic carbon nitride for the design of novel materials, offering exciting opportunities for next generation photocatalysts due to their synergetic interaction encompassing both interfacial electron transfer between the two constituent phases and the enhanced adsorption capacity.

2.2.1 Carbon Nanotubes (CNTs) Based Photocatalysts

Carbon nanotubes (CNTs) are graphite sheets rolled up into cylinders with diameters of the order of a few nanometers and up to some millimeters in length [36]. CNTs can be classified as single-walled CNTs (SWCNTs), double-walled CNTs (DWCNTs) and multi-walled CNTs

(MWCNTs) regarding to the number of carbon walls. MWCNTs are considered as concentric SWCNTs with increasing diameters and coaxially disposed, often up to several tens so that the external diameter can reach 100 nm [37]. Since the work published by Iijima in 1991 [38], CNTs have attracted a large interest in nanoscience and nanotechnology. CNTs are considered to be a good support material for photocatalysts, owing to their high specific surface area and high quality active sites, charge separation stabilization, retardation of electron-hole recombination by trapping electrons transferred from the semiconductor, and visible light response through band-gap modification [36, 39].

CNTs hybrid photocatalysts are widely applied in the photodegradation of organic pollutants [37]. However, there are a limited number of studies focused on the CO_2 reduction. In 2013, these studies were already reviewed by Sun and Wang [40]. **Table 3** summarizes the two additional works published since then and related with the photocatalytic reduction of CO_2 over CNT-based photocatalysts.

Table 3 - Recent works on photocatalytic reduction of CO_2 over CNT-based photocatalysts (selectivity to the desired product was not referred in these publications).

Catalyst	Light source	Reaction conditions	Major product (yield in μmol h^{-1} g^{-1})	Ref. (year)
20% CuO-MWCNT@TiO_2	15 W light bulb emitting visible light (λ > 400 nm)	Photocatalysts coated onto glass rods and then loaded into a quartz tube; mixture of CO_2 and water vapor	CH_4 (0.12)	[41] (2014)
20% Fe2O3-MWCNT@TiO2			CH_4 (0.1)	
20% NiO-MWCNT@TiO_2			CH_4 (0.06)	
20% CoO-MWCNT@TiO_2			CH_4 (0.05)	
20% ZnO-MWCNT@TiO_2			CH_4 (0.03)	
Bare MWCNT@TiO_2			CH_4 (0.09)	
Ag@ AgBr/CNT	150 W Xe lamp (λ > 420 nm) Irradiance (*I*) = 25 mW cm^{-2}	0.5 g catalyst; 100 ml of $KHCO_3$ (0.2 M); 7.5 MPa; room temperature	CH_4 (30) CH_3OH (18) CO (8) C_2H_5OH (3)	[42] (2013)

Gui et al. [43] prepared multi-walled carbon nanotubes@TiO_2 core shell nanocomposites (MWCNT@TiO_2) using a simple coating approach. The obtained yield of methane upon the reaction follows the order MWCNT@TiO_2 > MWCNT > Anatase TiO_2 under visible light irradiation. Photogeneration and trapping of electron–hole pairs at the surface vacancies generate a charge imbalance between the TiO_2 and MWCNT. Hence, trapped electrons migrate from the conduction band (CB) of TiO_2 to the neighboring MWCNT which has lower band-edge position, to achieve charge equilibrium (**Figure 6**). The movement of electrons to MWCNT reduce their recombination with holes in the lattice of TiO_2, maximizing the overall efficiency of the reaction.

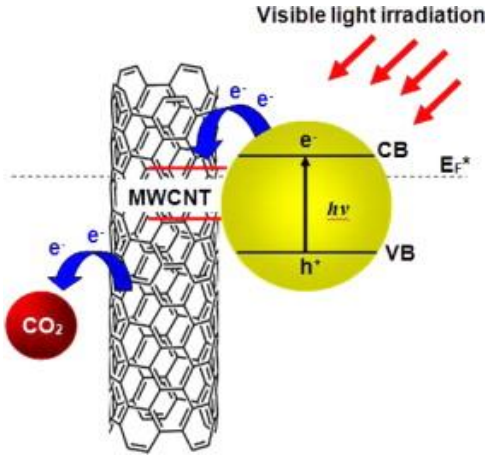

Figure 6 - Photoexcitation of the MWCNT/TiO_2 nanocomposites and the subsequent electron charge transfer. Reproduced with permission from Ref. [43]. Copyright (2014), American Chemical Society.

After this study, Gui et al. [41] prepared a series of multi-walled carbon nanotubes@TiO_2 core shell nanocomposites, loaded with common transition metal oxides, namely, iron (Fe_2O_3), copper (CuO), cobalt (CoO), zinc (ZnO) and nickel oxide (NiO), through incipient wetness impregnation. The CO_2 photoreduction test (in the same conditions of the previous work) demonstrated that CuO and Fe_2O_3-MWCNT@TiO_2 yielded higher methane formations, for 8 h of irradiation (**Table 3**). The other tested metal oxide loaded photocatalysts exhibited lower performances, relatively to the undoped-MWCNT@TiO_2. Results obtained with ZnO and NiO were in accordance with their optical properties, showing neither improvement in the visible light absorption nor red-shifting of the absorption band-edge positions. In the case of CoO-MWCNT@TiO_2 composites, an excellent charge separation ability was observed (fluorescence emission spectrum), but a lower methane formation was obtained. According to the authors, CoO itself is not active for CO_2 photoreduction. Regarding CuO- and Fe_2O_3-doped nanocomposites, the photoexcited electrons can be effectively transferred from the

TiO_2 lattice and trapped at the CuO and Fe_2O_3 dopants, thus impeding the surface charge recombination and facilitating the oxidation of OH^- and reduction of CO_2.

A plasmonic silver/silver bromide CNTs-based nanocomposite material (Ag@AgBr/CNT) was synthesized by Asi et al. [42]. The product yields were superior using Ag@AgBr/CNT nanocomposites with different CNT lengths than using Ag@AgBr crystals (**Figure 7**). The presence of CNTs in the nanocomposites, as electron acceptors, suppressed the charge recombination. It was also found that for longer CNTs, higher yields were registered, owing to better charge transport capacities. In this study, among other parameters, stability of the composites was also evaluated. After five repeated runs, the total yield of fuels remained about 85 % of the first cycle, proving the chemical stability of the catalyst.

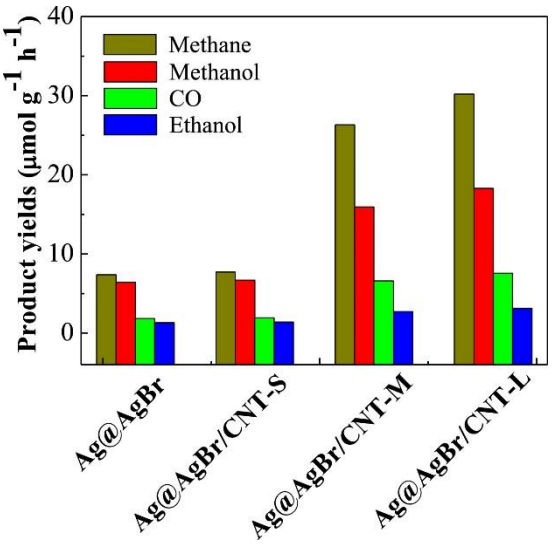

Figure 7 - Yield of photocatalytic products of Ag@AgBr and Ag@AgBr/CNT nanocomposites with different CNTs lengths (-S = Short; -M = Medium; -L = Long). Reproduced with permission from Ref. [42]. Copyright (2013), Elsevier.

2.2.2 Graphene-Based Photocatalysts

Graphene is a planar monolayer of carbon atoms arranged into a two-dimensional honeycomb lattice. Graphene possesses unique properties, such as a large theoretical specific surface area of 2,630 $m^2 g^{-1}$, high intrinsic charge mobility of 200,000 $cm^2 V^{-1} s^{-1}$, superior mechanical properties with Young's modulus of 1 TPa and exceptional thermal conductivity of 5,000 W $m^{-1} K^{-1}$ [39, 44-46]. Graphene oxide (GO) has attracted huge interest as a valuable precursor of graphene because oxygen functional groups attached on the graphene surface can be partly removed, resulting in the partial restoration of the sp^2 hybridization of carbon. The

exfoliation of graphite oxide, followed by a reduction process to yield reduced graphene oxide (rGO), offers important advantages, namely the possibility to obtain a tailored hydrophilic surface of graphene, decorated with oxygenated functionalities, using cost-effective approaches [47].

Graphene cannot be employed as an antenna or a light harvester, owing to its transparency against visible and UV light [44]. However, the hybrid of graphene can be combined with a semiconductor to exhibit photocatalytic activity. If the conduction band of a semiconductor is smaller than the work function of graphene (~4.5 eV) [48], the photo-generated electrons rapidly migrate to graphene, via a percolation mechanism, circumventing recombination with the holes generated on the semiconductor surface [49]. Furthermore, graphene-based nanocomposites increase the absorption of light intensity and extend the light absorption range, towards the visible part of the solar spectrum. Moreover, graphene-based photocatalysts present large surface areas, meaning that more surface active sites are available for the adsorption of reactants [45].

The photocatalytic performance of graphene-based composites have been mostly tested in the degradation of organic pollutants. Other less explored applications include the reduction of toxic metal ions in aquatic matrices, the photoinactivation of bacteria, water splitting and the CO_2 photoreduction to generate solar fuels [45]. Some relatively recent publications have already reviewed the use of graphene-based photocatalysts for CO_2 reduction [18, 21, 29, 40, 45]. The most recent works (not included in these reviews) are summarized in **Table 4**.

Table 4 - Recent work on photocatalytic reduction of CO_2 over graphene-based photocatalysts (selectivity to the desired product was not referred in these publications).

Catalyst	Light source	Reaction conditions	Major product (yield in μmol h^{-1} g^{-1})	Ref. (year)
Anatase TiO_2	15 W light bulb emitting visible light	Catalyst powder fixed into a quartz reactor; mixture of CO_2 and water vapor	CH_4 (0.021)	[50] (2015)
TiO_2 P25			CH_4 (0.022)	
rGO-TiO_2			CH_4 (0.109)	
Pt/rGO-TiO_2			CH_4 (0.283)	
Pd/rGO-TiO_2			CH_4 (0.199)	
Ag/rGO-TiO_2			CH_4 (0.166)	
Au/rGO-TiO_2			CH_4 (0.126)	
Cu_2O– 0.5 % rGO	150 W Xe lamp at visible light irradiation	0.5 g catalyst; 3 ml of DI water; Na_2SO_3 (0.7 M); batch reactions	CO (46*)	[51] (2014)
Cu_2O – rGO	Solar simulator with a 500 W Xe lamp	0.1 g catalyst; 100 ml of NaOH (0.1 M); room conditions	CH_3OH (4.15)	[52] (2014)
10 wt. % Cu-GO	300 W Ha lamp simulating solar light I = 100 mW cm^{-2}	0.1 g catalyst; mixture of CO_2 and water vapor	CH_3OH (1.47) CH_3CHO (1.94)	[53] (2014)
ZnO-rGO	Solar simulator with a 500 W Xe lamp	0.1 g catalyst; 100 ml of $NaHCO_3$ (0.0025 M); room conditions	CH_3OH (4.58)	[54] (2013)

* Yield given in ppm g^{-1}.

A set of noble metal (platinum, palladium, silver and gold) modified rGO-TiO_2 nanocomposites for the CO_2 conversion to methane under visible light was prepared by Tan et al. [50]. Methane production was markedly enhanced in the presence of the studied metals, following the order Pt/rGO-TiO_2 > Pd/rGO-TiO_2 > Ag/rGO-TiO_2 > Au/rGO-TiO_2 > rGO-TiO_2 > TiO_2 P25 ≈ anatase TiO_2. The incorporation of rGO sheets increased the electron

collection and transport, effectively separating the photogenerated charge carriers and increasing the photocatalytic activity. Regarding the presence of noble metal nanoparticles, the improvement of the photoactivity is attributed to the formation of a Schottky barrier at the metal–semiconductor interface, allowing the transfer of electrons from the conduction band (CB) of TiO_2 to the metal nanoparticles (**Figure 8**). Furthermore, the photoresponse spectrum was also widened. Platinum exhibited greater yield of methane, due to its higher working function, relatively to other employed noble metals. In this same report, the optimum platinum loading was found to be 2 wt. %. Lower contents did not have sufficient electron trap sites, while higher mass ratios could block the light absorption centers of TiO_2 or also increased the number of electrons on the surface of TiO_2, promoting consequent recombination with corresponding holes.

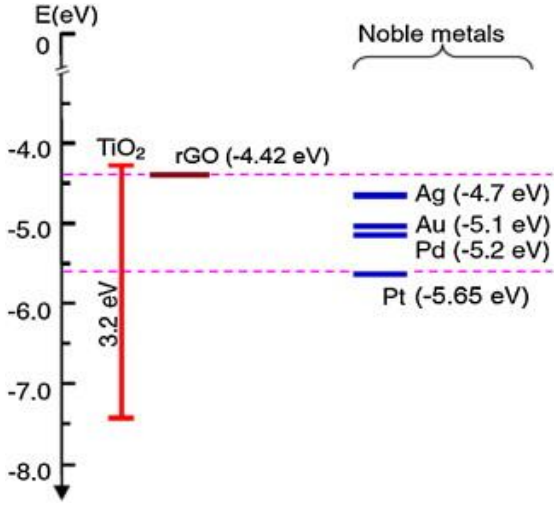

Figure 8- Energy band positions of rGO, Pt, Pd, Ag and Au, including the conduction and valence bands of TiO_2 photocatalyst. Reprinted with permission from Ref. [50]. Copyright (2015), Elsevier.

Nanocomposites of rGO-Cu_2O for the CO_2 conversion to carbon monoxide, under visible light irradiation were synthesized by An et al. [55], achieving approximately 0.34 % in quantum yield. CO formation rate was six-fold higher, when the rGO coating of Cu_2O was introduced. Wang et al. [52] also prepared rGO-Cu_2O nanocomposites, the methanol yield improving 53 % relatively to bare Cu_2O under illumination by simulated sunlight. Concerning both studies, the improved activity together with the enhanced stability of Cu_2O was attributed to the efficient charge separation and transfer to rGO. Despite having used the same photocatalyst, different products were obtained, namely, carbon monoxide and methanol. These studies were an excellent example of the CO_2 photocatalytic reduction complexity and difficulty to control product selectivity. There is a lack of understanding on the factors that control the product distribution. The exact mechanism of CO_2 photoreduction, reaction pathways and influence of reaction conditions still remains to be unraveled.

A series of GO loaded with different contents of copper nanoparticles (Cu NPs) were produced by Shown and co-workers [53]. The mass ratio of 10 % between Cu and GO demonstrated a good photocatalytic performance, reaching a total solar fuel formation of 6.82 μmol h^{-1} g^{-1}. In comparison with pristine GO and commercial P25, the reduction rates were superior 60 and 240 times, respectively. Due to the lower Fermi level of Cu NPs, comparatively to the conduction band of GO, the excited electrons spontaneously migrated from the GO CB to the Cu nanoparticles. As a result, charge carriers recombination was effectively hindered and photocatalytic CO2 reduction was enhanced.

The use of rGO-ZnO nanocomposites for CO_2 photoreduction to methanol, obtaining a production rate of 4.58 μmol g^{-1} h^{-1} was investigated by Li et al. [54]. Once again, the presence of rGO enlarged the light absorption spectrum (**Figure 9**) and minimized the recombination of photo-induced charge carriers (**Figure 10**).

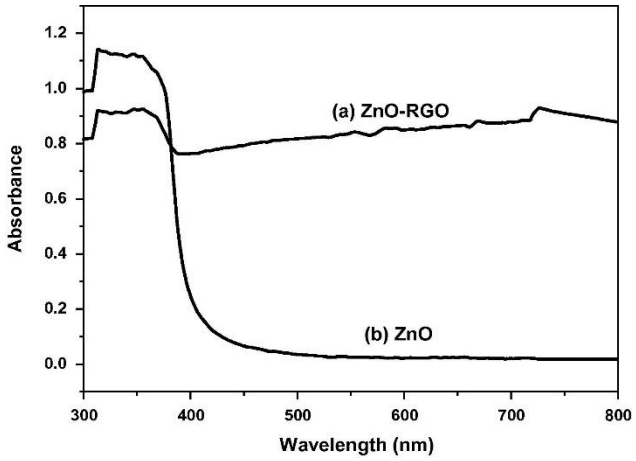

Figure 9 - UV–vis spectra of ZnO-RGO nanocomposites and ZnO particles. Reproduced with permission from Ref.[54]. Copyright (2013), Elsevier.

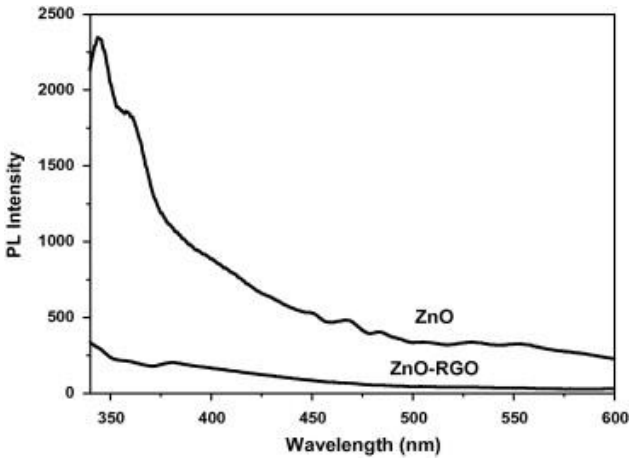

Figure 10 - Photoluminescence spectra of ZnO and ZnO-rGO composites with excitation wavelength of 325 nm. Reproduced with permission from Ref.[54]. Copyright (2013), Elsevier.

2.2.3 Graphitic Carbon Nitride-Based Photocatalysts

Carbon nitrides (C_3N_4) are a class of polymeric organic nonmetallic materials, consisting mainly of carbon and nitrogen. This category has five allotropes, including α-C_3N_4, diamond-like ß-C_3N_4, cubic-C_3N_4, pseudocubic-C_3N_4 and graphitic-C_3N_4 (g-C_3N_4). Among them, g-C_3N_4 is the most stable at ambient conditions, having a layered structure like graphene [56, 57]. g-C_3N_4 is a polymer based on tri-s-triazine units as elementary building blocks. The π-conjugated phase between the layers is responsible for the g-C_3N_4 high thermal and chemical

stability, potentiating its extensive applications in heterogeneous catalysis [57]. The band gap of g-C_3N_4 is around 2.7 eV, corresponding to a moderate absorption in the visible-light region [58]. Moreover, g-C_3N_4 is made up of a layered structure which can be fabricated by facile thermolysis methods from low-priced precursors, such as urea, thiourea, cyanamide, dicyandiamide and melamine [59, 60].

All of these properties make g-C_3N_4 for the widespread applications in the field of photocatalysis. The utilization of g-C_3N_4 is currently more reported in the degradation of water pollutants and H_2 generation [58]. Wang et al. [61] firstly reported polymeric g-C_3N_4 as an innovative photocatalyst that exhibited photoactivity for H_2 production from water splitting, under visible-light irradiation. An inferior number of studies were conducted towards CO_2 photocatalytic reduction. Thus, there is still a long way to go, before one reach reasonable efficiencies and large-scale implementation. Nevertheless, some strategies have already demonstrated significant potential to increase the photocatalytic yields of g-C_3N_4 for CO_2 photoreduction. **Table 5** compiles recent works within the g-C_3N_4 photocatalyst category toward CO_2 conversion.

Table 5 - Recent work on photocatalytic reduction of CO_2 over graphitic carbon nitride-based photocatalysts (selectivity to the desired product was not referred in these publications).

Catalyst	Light source	Reaction conditions	Major product (yield in μmol h^{-1} g^{-1})	Ref. (year)
Bulk g-C_3N_4	300 W Xe lamp visible light (λ > 400 nm) I = 200 mW cm^{-2}	20 mg catalyst; mixture of CO_2 and water vapor; pressure of 0.06 MPa	CH_3CHO (2.2)	[62] (2014)
g-C_3N_4 nanosheets			CH_4 (1.2)	
Urea derived g-C_3N_4	300 W Xe lamp visible light (λ > 420 nm) I = 267 mW cm^{-2}	0.2 g catalyst; 100 mL NaOH (1 M); supercritical CO_2; room conditions	CH_3OH (6.28) C_2H_5OH (4.51)	[63] (2013)
Melanine derived g-C_3N_4			C_2H_5OH (3.64)	
1 wt.% Pt/ g-C3N4	300 W simulated solar Xe arc lamp	0.1 g catalyst; 10 mL DI water; mixture of $NaHCO_3$ (0.12g) and HCl (0.25 mL, 4 M); room conditions	CH_4 (0.3) CH_3OH (0.23) HCHO (0.09)	[60] (2014)

Table 5 – Continued.

Catalyst	Light source	Reaction conditions	Major product (yield in μmol h^{-1} g^{-1})	Ref. (year)
0.5 wt.% Ag/ g-C_3N_4 + WO_3	LED lamp (λ = 435 nm) I = 3 mW cm^{-2}	3 mg catalyst; 5 mL ion-exchanged water saturated with CO_2; room conditions	CH_3OH (24.3)	[59] (2014)
0.5 wt.% Au/ g-C_3N_4 + WO_3			CH_3OH (34.73)	
2 wt. % Pt- g-C_3N_4	15 W energy saving light bulb at visible light irradiation I = 8.5 mW cm^{-2}	Mixture of CO_2 (5 mL min^{-1}) and water vapor; room conditions	CH_4 (1.30)	[64] (2015)
0.12 wt. % S/ g-C_3N_4	300 W simulated solar Xe arc lamp	0.1 g catalyst; 10 mL DI water; Mixture of $NaHCO_3$ (0.12 g) and HCl (0.25 mL, 4 M); Room Conditions	CH_3OH (0.37)	[57] (2015)
6 wt.% ZnO/ g-C_3N_4	500 W Xe lamp (λ > 420 nm) I = 105 mW cm^{-2}	10 mg catalyst; Mixture of CO_2 and water vapor; P=0.4 MPa; T= 80 °C	CO (5.1) CH_3OH (0.5)	[65] (2015)
30 mol % Ag_3PO_4/ g-C_3N_4	500 W Xe lamp (λ > 420 nm) I = 105 mW cm^{-2}	10 mg catalyst; Mixture of CO_2 and water vapor; P=0.4 Mpa; T= 80 °C	CO (44) CH_3OH (8)	[66] (2015)

The control of the band-structure of two g-C_3N_4 photocatalysts with different band structures was reported by Niu et al. [62], namely for bulk g-C_3N_4 and g-C_3N_4 nanosheets with bandgaps

of 2.77 eV and of 2.97 eV, respectively, with different influences in the product selectivity for CO_2 photoconversion. The major products obtained using bulk g-C_3N_4 and g-C_3N_4 nanosheets are acetaldehyde (CH_3CHO) and methane (CH_4), respectively (**Figure 11**).

The nanosheets of g-C_3N_4, with larger bandgap, can provide a stronger driving force for the transfer of electrons and holes, due to the higher energetic difference between the electronic band edges and the redox potentials of the reactants. Consequently, faster and long-lived electrons and holes are transferred to the intermediate species and involved in the elementary steps of CH_4 formation. Another important parameter is the higher specific surface area of the nanosheets (306 and 50 $m^2\ g^{-1}$ for nanosheets of g-C_3N_4 and bulk g-C_3N_4, respectively) providing abundant active sites for the adsorption of intermediate species and, thus, promoting the subsequent elementary steps towards methane formation.

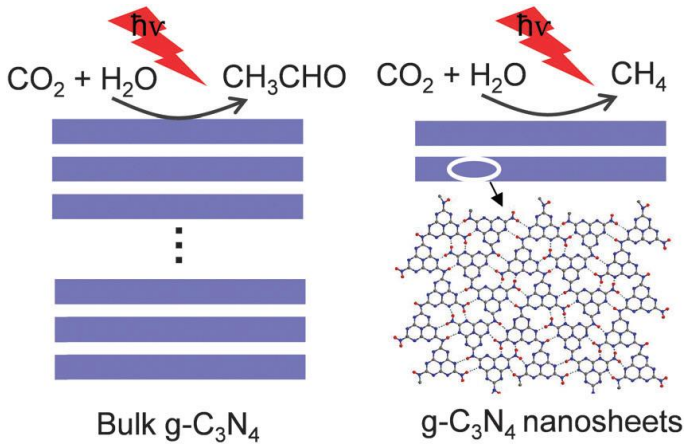

Figure 11- Schematic of the generation of CH_4 and CH_3CHO on bulk g-C_3N_4 and g-C_3N_4 nanosheets in the photoreduction of CO_2 in the presence of water vapor. Reproduced with permission from Ref. [62]. Copyright (2014), Royal Society of Chemistry.

Two types of graphitic carbon nitride were synthesized through a pyrolysis process of urea (u-g-C_3N_4) or melamine (m-g-C_3N_4) by Mao et al. [63]. These photocatalysts exhibited different activity and selectivity on the formation of CH_3OH and C_2H_5OH in an aqueous suspension, under visible-light irradiation. Compared with m-g-C_3N_4, u-g-C_3N_4 has a larger surface area and higher photocurrent in suspension, showing a better performance for CO_2 photocatalytic reduction. The different photocatalytic activities and selectivities for the formation of organic fuels during CO_2 photoreduction is probably due to the differences in the crystallinity and microstructure of u-g-C_3N_4 and m-g-C_3N_4.

There have also been various modifications to graphitic carbon nitrides targeting improved solar fuels yields. Yu et al. [60] and Ong et al. [64] prepared a set of g-C_3N_4 photocatalysts loaded with platinum nanoparticles. Both studies revealed an enhancement on the photocatalytic performance of g-C_3N_4. In the first report, platinum acted as an effective co-

catalyst, which affected the photocatalytic activity and also influenced the selectivity of the product generation (**Figure 12)**. Relatively to the second, methane formation was accelerated by the presence of the noble metal, reaching its maximum for a corresponding weight content of 2 %. The remarkable photocatalytic activities of Pt/g-C_3N_4 nanostructures was ascribed to the enhanced visible light absorption and efficient interfacial transfer of photogenerated electrons from graphitic carbon nitride to platinum nanoparticles, as evidenced by the UV-Vis, photoluminescence and transient photocurrent response studies.

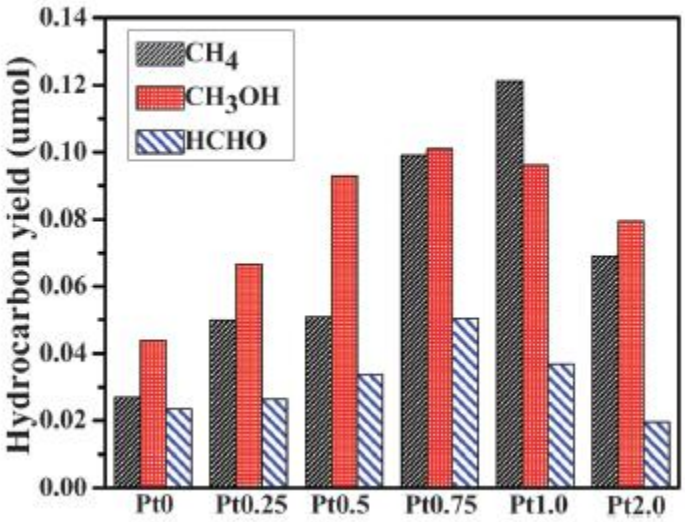

Figure 12 - Influence of the platinum content on the photocatalytic performance of g-C_3N_4. Reproduced with permission from Ref. [60] Copyright (2014), Royal Society of Chemistry.

Recently, a series of ZnO nanoparticles functionalized g-C_3N_4 sheets was prepared following an impregnation method by He et al. [65]. The interactions between the two components promoted the formation of a hetero-junction structure in the composite, inhibiting the recombination of electron–hole pairs and, finally, enhancing the photocatalytic performance.

The CO_2 photocatalytic reduction performance of undoped and sulfur-doped g-C_3N_4, fabricated by simple thermolysis of melamine and thiourea at 520 ºC, respectively, was reported by Wang et al. [57]. It was found that the CH_3OH yield over the unit area of the samples fabricated with thiourea was nearly 2.5 times superior to the product derived from melamine. The authors suggested that the better performance of the sulfur-doped g-C_3N_4 is attributed to the presence of defects in the structure of this material. Furthermore, these structural defects play the role of trapping photogenerated electrons, inducing charge transfer and separation with the consequent life time prolongation. **Figure 13** depicts the transient photocurrent responses of both materials. The sample synthetized from thiourea

(TCN) exhibited higher photocurrent and photoactivity than melamine (MCN), owing to the existence of more defects that contributed to the promotion of photogenerated charge carrier separation.

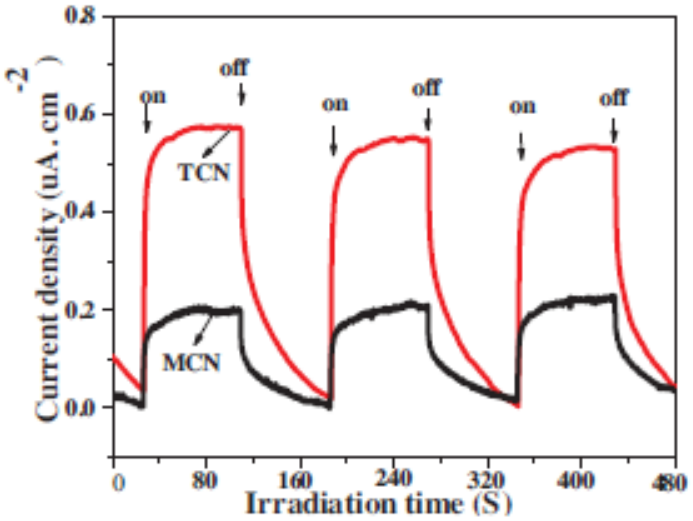

Figure 13 - Transient photocurrent responses of TCN and MCN. Reproduced with permission from Ref. [57] Copyright (2015), Elsevier.

2.3 Water as Reducing Agent

The photocatalytic reduction of CO_2 into hydrocarbon fuels requires a reducing compound, acting as the hydrogen source. Among the various possibilities, the ideal but scientifically more challenging is H_2O as the reducing agent, that upon oxidation to molecular dioxygen should provide the hydrogen atoms that will incorporate CO_2 and form the desired products, viz. methanol and methane [67].

As the most oxidized state of carbon, CO_2 can only be reduced. Inversely, water can play the role of reductant, generating O_2, or an oxidant agent, forming H_2. The reduction potential of H_20 to produce H_2 is inferior ($E°_{red}$ = 0 V) than the standard reduction potential of CO_2 to generate $CO_2^{\bullet -}$ ($E°_{red}$ = -1.9 V). Hence, H_2O simultaneously quenches positive holes in the semiconductor valence band and competes advantageously with CO_2 for the photogenerated electrons reaching the conduction band. Generally, hydrogen formation is larger than the total amount of products formed by CO_2 photoreduction [68]. In spite of having dual behavior, water (either in aqueous or gas phase system) remains the standard hydrogen source.

In an aqueous system, the pH level is a vital factor, considering its influence in the chemical form of CO_2 dissolved in water and solubility. CO_2 partially hydrates in water to carbonic acid (H_2CO_3). H_2CO_3 may lose up to two protons through the acid equilibria described by Equations **8** and **9**

(8) $CO_2 + H_2O \rightleftharpoons H_2CO_3 \leftrightarrow H^+ + HCO_3^-$ $\quad pK_a = 6.4$

(9) $HCO_3^- \rightleftharpoons H^+ + CO_3^{2-}$ $\quad pK_a = 10.3$

At acidic pH, well below 6.4, the predominant carbon species is H_2CO_3. When pH ranges between 6.4 and 10.3, HCO_3^- ions are the prevalent form. Lastly, at more alkaline pH level, much higher than 10.3, CO_2 is present in the form of CO_3^{2-} ions, as shown in **Figure 14**.

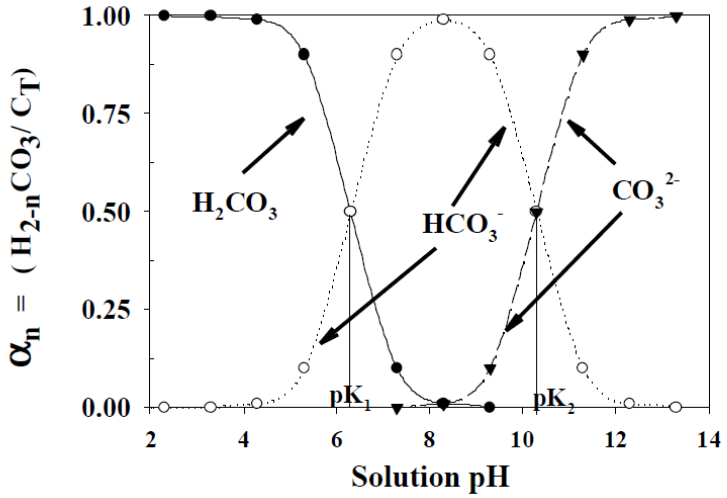

Figure 14 - Distribution of carbonate species as a fraction of total dissolved carbonate in relation to solution pH. Reprinted from Ref. [69].

Carbonate and bicarbonate species are more difficult to reduce than CO_2 [9]. Moreover, CO_3^{2-} ions are good hole quenchers and may be easily oxidized, inverting the overall process [68]. In contrast, the dissolved CO_2 level in water decreases at acidic pH. Although, low pH favors H^+ supplying, it should be noted that the low concentration of H_2CO_3 dissolved in the solution is a limiting factor.

The photocatalytic reduction of CO_2 at different pH, using a graphene-TiO_2 composite was tested by Zhang et al. [70], which concluded that the optimal yields of formic acid and methanol were obtained at neutral pH (**Figure 15**). On the other hand, the lowest yields were obtained at alkaline condition (pH 13). According to the authors, the negatively charged CO_3^{2-} species were more likely to be expelled by the negatively charged surface of the catalyst, as compared with the HCO_3^- species. In turn, at acidic pH, although H^+ ions

could be abundantly supplied, the dissolved CO_2 levels in water were only ca. 0.0021 mol/L, contrasting with the 0.033 and 0.108 mol/L values at pH 7 and 13, respectively.

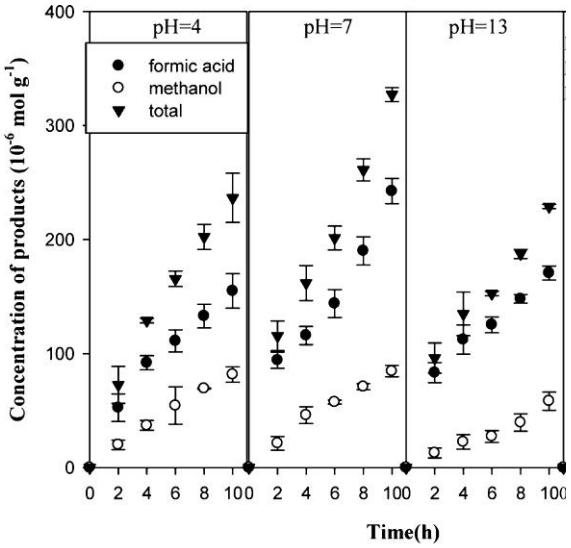

Figure 15 - Photocatalytic reduction of CO_2 at different pH, using a graphene-TiO_2 composite. Reproduced with permission from Ref. [70]. Copyright (2015), American Chemical Society Publications.

The influence of the initial pH on the yield of photocatalytic products on a silver bromide - titanium dioxide ($AgBr/TiO_2$) catalyst was analysed by Asi et al. [71]. Results are shown in **Figure 16**. It was found that the product yield increased with the pH value to 8.5. Once again, a relatively higher photocatalytic reduction activity was achieved in the neutral and weak alkaline pH range, representing the overall combined effect of the higher concentration of OH^- ions and lower electrostatic repulsive force between CO_2 species and the catalyst [71].

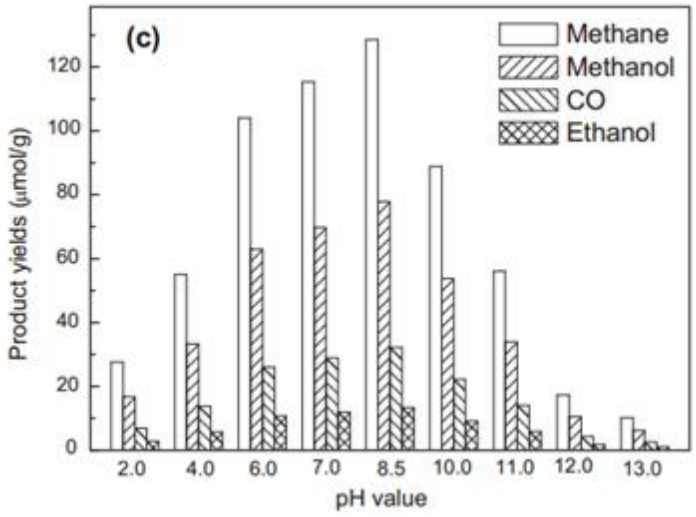

Figure 16 - Influence of the initial pH level in the photocatalytic reduction of CO_2, using $AgBr/TiO_2$. Reproduced with permission from Ref. [71]. Copyright (2011), Elsevier.

In order to avoid the above-mentioned problems, it could be advantageous to work under gas phase conditions. These systems involve the previous bubbling of CO_2 into water and subsequently the reactant mixture is fed into the reactor which is irradiated. However, in this case (solid-gas system), the photocatalyst needs to be immobilized [72]. The main advantages of this method are the easier separation of products, reactants and photocatalyst, as well as the possibility of overcoming the low solubility of CO_2 verified in aqueous systems and the absence of competition for electrons between water and CO_2.

2.4 Other Electron Donors

Due to fast recombination of photoelectrons in the conduction band and photoholes in the semiconductor valence band, it is very difficult to achieve an appreciable CO_2 photoreduction using water. The employment of better electron donors to react with the valence band photoholes may hinder the electron/hole recombination, resulting in higher quantum yields and more possibilities to reduce CO_2. These additives, also known as hole scavengers, are usually organic or inorganic reducing agents. Their function is to donate electrons, trapping holes in the semiconductor and undergoing oxidation. These compounds are more difficult to reduce than water, thus they will not promote competition with CO_2 for electrons in the conduction band. **Table 6** depicts some examples of other electron donors applied in liquid or gas phase reactions.

Liu et al. [73] studied the influence of sodium hydroxide (NaOH) and verified that its effect was significant in the photoreduction of CO_2, using titania supported cobalt phthalocyanine catalysts. OH^- ions could act as a strong hole scavengers and form OH radicals, reducing the recombination of hole-electron pairs. It was found that the product yield increased, when the concentration of NaOH increased up to 0.15 M. Contrariwise, for higher concentrations, total product formation was considerably diminished, due to the greater amount of OH radicals, which could oxidize the species in the reactor.

Table 6 – Examples of electron donors applied in liquid or gaseous phase.

Reaction Type	Reductants	Reference
Liquid-Phase	Sodium Hydroxide	[74-76]
	Sodium Bicarbonate	[71, 77]
	Sodium Sulphite	[73, 78, 79]
	Triethanolamine	[80-83]
	Triethylamine	[84, 85]
	Methanol	[86-88]
	Isopropyl alcohol	[89, 90]
Gas-Phase	Hydrogen	[91-94]
	Hydrogen Sulfide	[95]
	Methane	[96, 97]

The synergistic effect between NaOH and sodium sulphite (Na_2SO_3) was also investigated in this study. The influence of Na_2SO_3 on the yield of several products is shown in **Figure 17**. Clearly, the photocatalytic activity increased with the concentration of this hole scavenger. Though, when the Na_2SO_3 concentration surpassed 0.1 M, product formation was constant, considering the fact that the oversupply of electrons by Na_2SO_3 exceeded the need of holes in NaOH solution.

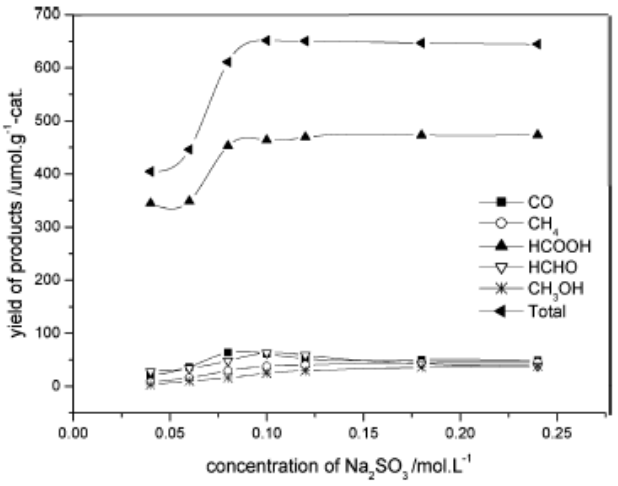

Figure 17 - The influence of Na_2SO_3 concentration on the product yield. Reproduced with permission from Ref. [73]. Copyright (2007). Royal Society of Chemistry.

The formation of CO_2 photocatalytic reduction products, on zinc sulphide – montmorillonite (ZnS-MMT) composite catalysts, with different reaction media was evaluated by Reli et al. [79]. It was verified that NaOH gave better yields of methanol than ammonium hydroxide (NH_4OH), owing to the higher solubility of CO_2 in the former (stronger base). When Na_2SO_3 was introduced in the reaction medium, the yield of methanol in the liquid phase increased. This result was ascribed to the primary oxidation of sulphite to sulphate, instead of the oxidation of methanol. In fact, the reverse oxidation of generated methanol back to CO_2 was prevented by the addition of Na_2SO_3.

An investigation to study the effects of different solvents on CO_2 photoreduction was carried out by Liu et al. [90]. TiO_2 nanoparticles embedded into SiO_2 were spin-coated onto a quartz plate, illuminated upon immersion in a suspension containing water or other solvents as acetonitrile, 2-propanol, propylene carbonate and dichloromethane with various dielectric constants. The two detected formed products were formate and carbon monoxide. The yield of formate increased with an increase in the dielectric constant of the employed solvent. When solvents of high dielectric constant such as water and propylene carbonate were employed, the formed $CO_2^{\cdot-}$ anion radicals may have been stabilized by the solvents, resulting in weak interaction with the photocatalyst surfaces [90].

In a recent study conducted by Wu et al. [98] the photocatalytic reduction of CO_2 to form methane (CH4), in a monoethanolamine (MEA) solution, was investigated by a mesoporous photocatalysts of Ti−MCM-41. The MEA solution was selected as the reductant, owing to its capacity to capture and absorb CO_2 from flue gas streams. The photocatalytic results of methane yields indicated that MEA was a better reductant, relatively to water and NaOH, the most frequently used reagents in CO_2 photocatalytic reduction systems. The performance of MEA solution may arise the concept of integrating the CO_2 capture and conversion, into a single process.

3 Experimental Section

3.1 Chemicals

The list of reagents used in the present work (and respective suppliers) is shown in Table 7.

Table 7 – Reagents employed in the catalysts preparation and CO_2 reduction experiments.

Supplier	Reagents
Sigma-Aldrich Corporation	Graphite flakes (particle size ≤ 20 μm)
	Ammonium hexaflurorotitanate (IV) ($(NH_4)_2TiF_6$, > 99.99%)
	Boric acid (H_3BO_3, > 99%)
	Sulphuric acid (H_2SO_4, > 95%)
	Hydrochloric acid (HCl, > 37 % w.w.)
	Potassium hydrogen phthalate ($KHC_8H_4O_4$, > 99.95%)
	Copper (II) nitrate trihydrate ($Cu(NO_3)_2.3H_2O$, > 98%)
	Titanium Dioxide P25 (TiO2, > 99.5 %)
	Sodium phosphate monobasic (NaH_2PO_4, > 99.0%)
	Sodium phosphate dibasic (Na_2HPO_4, > 99.95%)
	Sodium Hydroxide (NaOH, > 97%)
Alfa Aesar	Dihydrogen hexachloroplatinate(IV) hexahydrate ($H_2PtCl_6.6H_2O$, > 99.9%)

3.2 Synthesis of Graphene Oxide

The starting material graphene oxide (GO) was synthesized by oxidative treatment of synthetic graphite, following the modified Hummers method [99, 100] as described elsewhere [101]. For its synthesis, 50 mL of H_2SO_4 was added gradually with stirring and

cooling to a 500 mL flask containing 2 g of graphite. Then, 6 g of potassium permanganate ($KMnO_4$) was added slowly to the mixture. The suspension was constantly stirred for 2 h at 35 ºC. Subsequently, it was chilled in an ice bath and diluted by 350 mL of deionized water. Then, H_2O_2 (30 % w/v) was added in order to reduce residual permanganate to soluble manganese ions and a brilliant yellow product was formed. The oxidized material was washed with a 10 % HCl solution and then the suspension was filtered, washed several times with water until reach a neutral pH in the resulting water, and dried at 60 ºC for 24 h to obtain graphite oxide. The formed material was dispersed in water with subsequent exfoliation in an ultrasound bath (UP400S, 24 kHz) for 1 h. Finally, the resulting sonicated dispersion was centrifuged for 20 min at 3000 r.p.m. in order to obtain a suspension of graphene oxide.

3.3 Preparation of Graphene Oxide-TiO_2 Composite

Graphene oxide-TiO_2 (GOT) was prepared by the liquid phase deposition method (LPD) at room temperature by the introduction of graphene oxide, as described elsewhere [102, 103]. In this process, ammonium hexafluorotitanate (IV), NH_4TiF_6 (0.1 mol L^{-1}), and boric acid, H_3BO_3 (0.3 mol L^{-1}), were added to the carbon material suspensions and heated at 60 ºC for 2 h under continuous stirring. The materials were washed with water and dried at 100 ºC under vacuum for 2 h followed by a post-treatment under N_2 atmosphere at 200 ºC. The carbon loading was ca. 4 wt. %, taking into account the optimum photocatalytic activity obtained with these composites for the degradation of water pollutants [102, 103]. Bare TiO_2 was also prepared and treated by the same method, without the addition of any carbon material (referred as TiO_2). The photocatalyst from Evonik Degussa Corporation (P25) was also used and consist of both anatase (ca. 80 %) and rutile (ca. 20 %) crystalline phases.

3.4 Preparation of Bimetallic Loaded Catalysts

Bimetallic catalysts were prepared using both P25 and GOT by incipient wetness co-impregnation from aqueous solutions of the corresponding metal salts, $H_2PtCl_6.6H_2O$ and $Cu(NO_3)_2.3H_2O$ (**Figure 18**). The contents of Pt and Cu were fixed at 1%Pt–1%Cu (weight percentages). The catalysts were treated under air for 2 h and subsequently reduced under H_2 atmosphere for 4 h (both at 300 ºC). The composites prepared with P25 or GOT were designed as Pt-Cu/P25 and Pt-Cu/GOT, respectively.

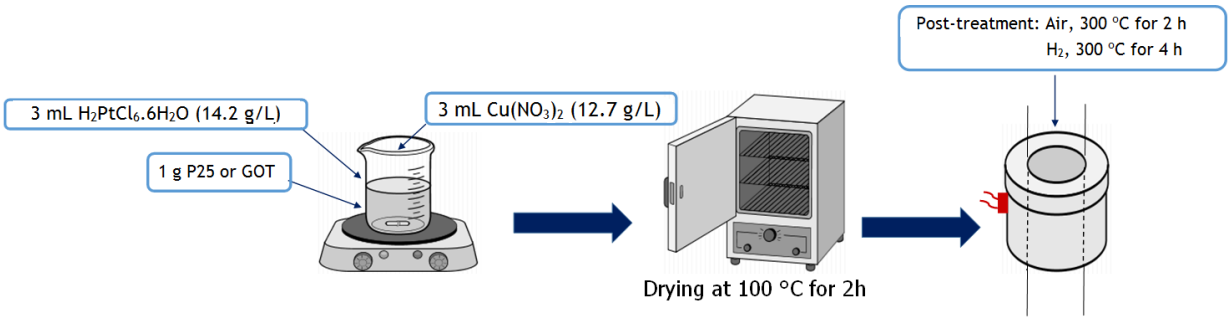

Figure 18 - Schematic representation of the procedure used for preparation of bimetallic catalysts (Pt-Cu/P25 and Pt-Cu/GOT).

3.5 Catalyst Characterization

Textural characterization of the materials was obtained from the nitrogen adsorption-desorption isotherms determined at -196 ºC (77 K) in a Quantachrome NOVA 4200e multi-station apparatus. The apparent surface area (S_{BET}) was determined by applying the Brunauer-Emmett-Teller (BET) equation [104].

Temperature programmed reduction (TPR) characterization was carried out in an AMI-200 (Altamira Instruments) apparatus; the sample (120 mg) was heated at 5 ºC min^{-1} up to 600 ºC under a flow of 5 % (v/v) H_2 diluted with He (total flow rate of 30 cm^3 min^{-1}).

The morphology of the composites was studied by scanning electron microscopy (SEM) in a FEI Quanta 400FEG ESEM/EDAX Genesis X4M instrument.

Attenuated total reflection Fourier transform infrared (ATR-FTIR) spectra were recorded on a NICOLET 510P FTIR spectrometer using ZeSn as ATR crystal.

The UV-Vis spectra of the solid powder materials were measured on a JASCO V-560 UV-Vis spectrophotometer equipped with an integrating sphere attachment (JASCO ISV-469). Barium sulphate was used as a reference. The spectra were recorded in diffuse reflectance mode and transformed by the instrument software to equivalent absorption Kubelka-Munk units. The band gap of the photocatalyst was determined using the Kubelka–Munk units as a function of the energy.

3.6 Photocatalytic CO_2 Reduction Experiments

The photocatalytic experiments for the reduction of CO_2 were carried out in a 300 ml glass immersion photochemical reactor (**Figure 19**).

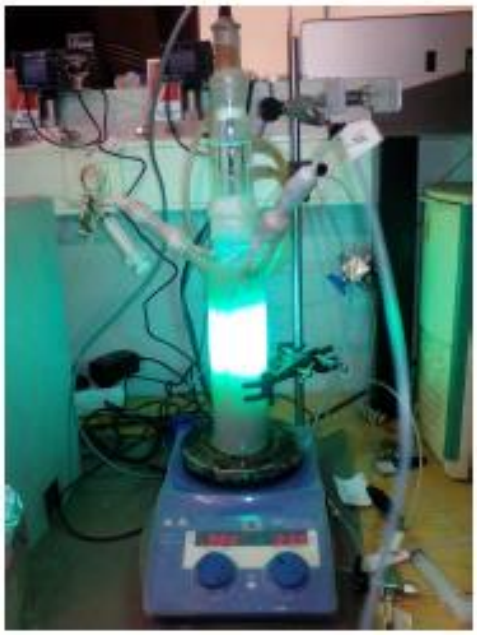

Figure 19 - Photocatalytic reaction setup.

The photoreactor was equipped with a UV-Vis Heraeus TQ 150 medium-pressure mercury vapor lamp (λ_{exc} = 254, 313, 365, 436, 546 and 578 nm) located axially in the reactor and held in a quartz immersion tube with water recirculation to maintain the temperature at around 25 ºC. A DURAN 50® glass cooling jacket was used for irradiation in the near-UV to visible light range, as depicted in **Figure 20** (main resulting emission lines λ_{exc} = 365, 436, 546 and 578 nm).

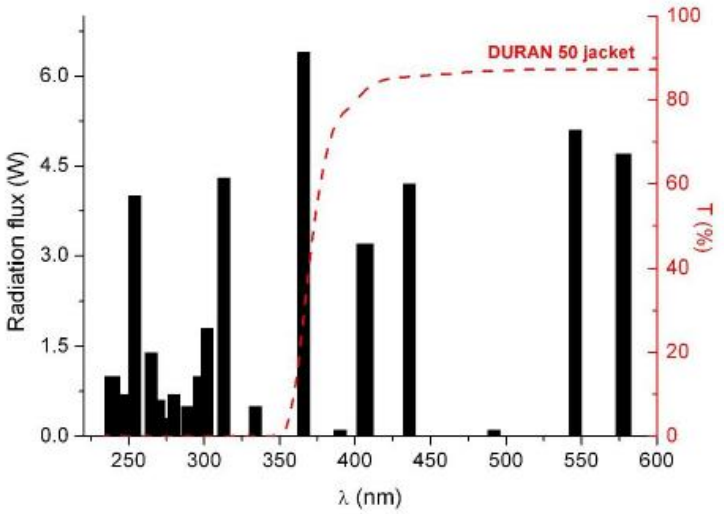

Figure 20 – Irradiance spectra of the Heraeus TQ-150 UV-Vis lamp equipped with a DURAN 50 ® jacket and transmittance spectrum of the cut-off filter.

In a typical run, the photoreactor was loaded with 250 ml of a solution (**Table 8**) and 250 mg of catalyst, i.e. a catalyst load of 1 g L^{-1}. Thus, the experiments were performed at neutral pH (7.0) and also at acidic (3.0) and alkaline (13.0) pH values. A pH of 3 was obtained with a buffer composed of potassium hydrogen phthalate and hydrochloric acid; pH 7 with monobasic sodium phosphate and dibasic sodium phosphate; and pH 13 with potassium chloride and sodium hydroxide.

Table 8 – Composition of the solutions used in the photocatalytic reactions.

Initial pH	Solution composition
3	173 mL $KHC_8H_4O_4$ (0.1 M) + 77 mL HCl (0.1 M)
7	98 mL NaH_2PO_4 (1 M)+ 152 mL Na_2HPO_4 (1 M)
13	50 mL KCl (0.2 M)+ 132 mL NaOH (0.2 M)

Prior to the illumination, the system was degased by using a He flow overnight (7 cm^3 min^{-1}). After the purging process, He and CO_2 flow rates were increased to 27 cm^3 min^{-1} and 3 cm^3 min^{-1}, respectively. The light source was then turned on and the photocatalytic reaction lasted for approximately 3 h under continuous magnetic stirring to prevent the sedimentation of the catalyst powder. To perform the evaluation of the liquid phase reaction products, small aliquots of the suspension were periodically withdrawn by using a syringe, filtered through Millipore membranes (0.45 μm) and then analyzed by gas chromatography (DANI GC-1000) using a capillary column (WCOT Fused Silica 30 m, 0.32 mm i.d., coated with CP-Sil 8 CB low bleed/MS 1 m film) and a flame ionization detector (FID). The gas phase was monitorized by a gas chromatograph (GC) coupled on-line with the reactor and equipped with a thermal conductivity detector (TCD), using a capillary column (Carboxen 1010 Plot. Supelco).

4 Results and Discussion

4.1 Photocatalysts Characterization

4.1.1 N_2 Adsorption-Desorption Isotherms

Nitrogen adsorption isotherms at -196 ºC were obtained and used in the determination of the surface area of the catalyst samples. Representative N_2 adsorption-desorption isotherms for both Pt-Cu/P25 and Pt-Cu/GOT materials are shown in **Figure 21**.

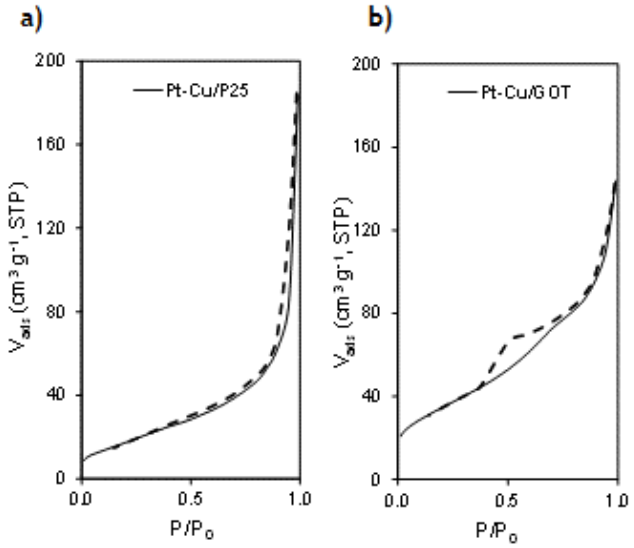

Figure 21 - N_2 adsorption-desorption isotherms at −196 ºC for Pt-Cu/P25 and for the Pt-Cu/ GOT composites.

Pt-Cu/P25 composite presented a S_{BET} lower than that of Pt-Cu/GOT (60 $m^2 g^{-1}$ and 111 $cm^3 g^{-1}$, respectively). It is interesting to note that the surface area of the bimetallic catalysts was considered to remain practically unchanged compared to the unloaded catalysts (**Table 9**).

Table 9 - BET surface area (SBET), relative amount of anatase and rutile crystalline phases and the band-gap energy (Ebg) of catalysts

Catalyst	S_{BET} /(± 10 m^2g^{-1})	Crystalline phase (%)*	E_g (eV)
P25	50	80 (A) / 20 (R)	3.18
Pt-Cu/P25	60	80 (A) / 20 (R)	2.22
GOT	120	100 (A)	2.98
Pt-Cu/GOT	110	100 (A)	--

* A: anatase; R: rutile.

4.1.2 Temperature Programmed Reduction

The TPR profile obtained for the bimetallic Pt-Cu/P25 catalyst is shown in **Figure 22**. The results show a single peak centered at ca. 250 ºC. This temperature for maximum H_2 consumption rate lies between those of monometallic Pt and Cu samples, as previously reported [105]. Thus, the single peak suggests an interaction between the Pt and the Cu species in the sample, which have influence in the reducibility of these species. This was also observed in the literature for Au-Cu [106] and Au-Pd [107] systems. According to these results, the catalysts were treated at 300°C to assure an effective reduction of the metals.

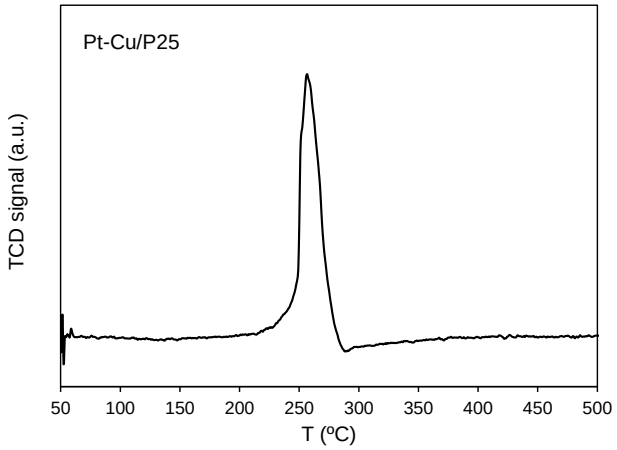

Figure 22 - TPR profiles of the Pt-Cu/P25 catalyst.

4.1.3 Scanning Electron Microscopy

The representative SEM images of P25, GOT composite, as well as, the Pt-Cu/loaded photocatalysts are shown in **Figures 23a-f.** The GOT composite consists of TiO_2 particles aggregated on the GO layers, forming GOT platelets (**Figure 23a**) with a well TiO_2 distribution on both sides of the GO nanosheets [108]. The morphology of P25 consists of small aggregated particles of anatase and rutile crystalline phases (**Figure 23b** and **Table 9**). The morphology observed for Pt-Cu/GOT (**Figure 23c**) was different than that observed for GOT (**Figure 23a**), since the platelets were not so notorious when the metals were loaded. **Figure 23d** shows the image recorded with backscattered electrons which allows a better visualization of the metal nanoparticles. The surface morphology of the Pt-Cu/P25 photocatalyst (**Figure 23e**) seems to be similar to that of P25 (**Figure 23b**). The EDS spectrum obtained for the Pt-Cu/P25 composite (**Figure 23f**) revealed the presence of Ti and O and confirms the Cu and Pt loading.

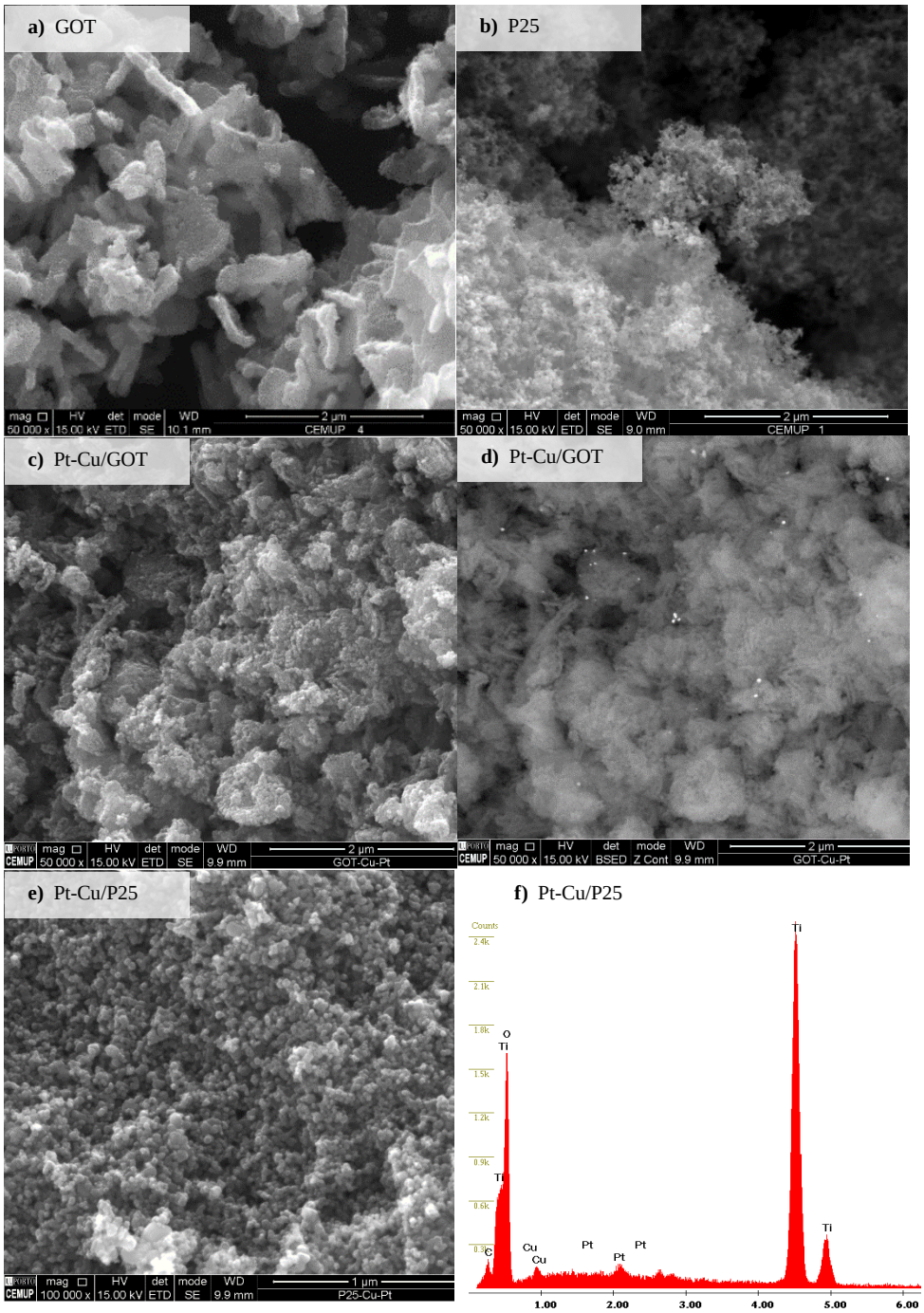

Figure 23 - SEM images of GOT (a), P25 (b), Pt-Cu/GOT (c,d) and Pt-Cu/P25 (e). SEM images recorded with backscattered electrons detection of Pt-Cu/GOT (d) EDS spectrum of Pt-Cu/P25 (f).

4.1.4 Attenuated Total Reflection Fourier Transform Infrared

ATR-FTIR spectra of GO, P25 and GOT, as well as the respective Pt-Cu loaded catalysts are depicted in **Figure 24**. These spectra show a broad band situated between 2800 and 3600

cm^{-1}, associated with stretching vibrations of water molecules and hydroxyl groups. This is confirmed by the presence of some bands around 1620 and 1685 cm^{-1} caused by bending vibration of coordinated water although the presence of Ti-OH bonds could also have certain contribution to this peak [109, 110] The band corresponding to the vibration of Ti-O-Ti bonds was situated between 800 and 950 cm^{-1} [111].

In the case of GO, a broad band situated around 3000-3500 cm^{-1} is assigned to the vibration of C-OH groups. The absorption band at 1720 cm^{-1} is attributed to carbonyl groups, C=O. The band at around 1300-1370 cm^{-1} corresponds to C-OH stretching. The band at 1220 cm^{-1} corresponds to breathing vibrations of epoxy groups (-O-) and the band at 1050 cm^{-1} is attributed to the stretching vibration of C-O groups [112]. The intensity of the peak associated to C-O (hydroxyl and epoxy) decreased significantly in the GOT composite, suggesting TiO_2 anchoring to GO preferentially through these sites. The absorption band at around 1600 cm^{-1} can be assigned to the skeletal vibration of graphene sheets.

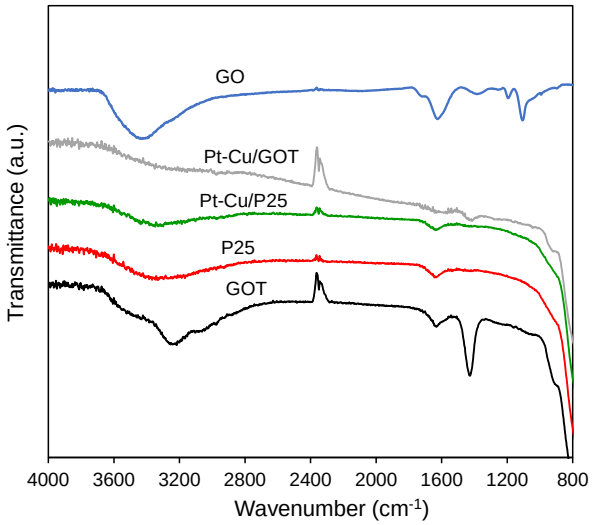

Figure 24- ATR spectra of GO, P25, GOT and the Pt-Cu loaded catalysts.

4.1.5 Diffuse Reflectance UV-Vis Spectra

The diffuse reflectance UV-Vis spectra of selected photocatalysts expressed in terms of Kubelka-Munk absorption units, are depicted in **Figure 25**. The UV-Vis spectra for the samples show the characteristic absorption sharp edge rising at 400 nm, due to the bandgap transition of the TiO_2 semiconductor. P25 exhibited no absorption above its absorption edge, indicating that will not present photocatalytic response in the visible light region. In contrast, the increase in absorption shown by the GOT composite in the visible spectral range is ascribed to the inherent light absorption capacity of carbon materials and also to the

possibility of being photoexcited, in this way promoting electronic transitions between carbon and TiO_2 phases [113, 114]. For the Pt-Cu/P25 catalyst, the band edge is expanded into both UV and visible regions. This effect can be related to the charge transfer transitions between the metal ions electrons and the TiO_2 conduction band [115].

Although the determination of bandgaps is difficult due to the significant increase of the background absorption above 400 nm, the transformed Kubelka-Munk function was plotted as a function of the energy of light as shown in **Figure 25 - inset**. The band gaps were estimated as 3.10, 2.98 and 2.20 eV for P25, GOT and Pt-Cu/P25, respectively (**Table 9**).

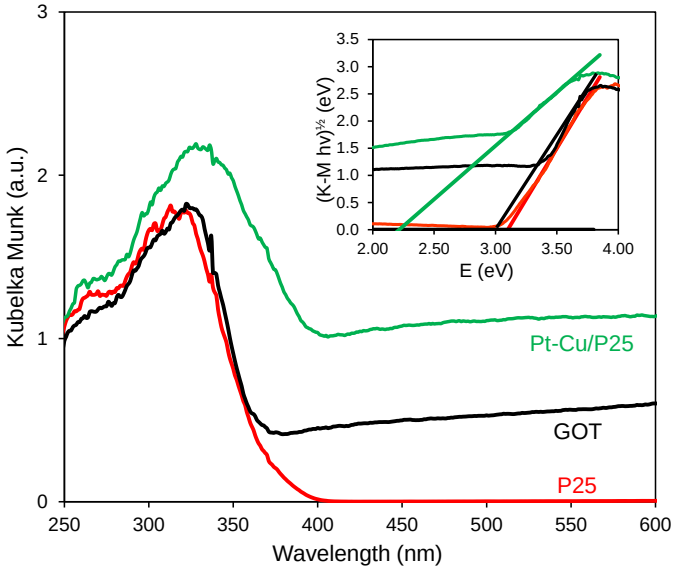

Figure 25- DRUV-Vis spectra of P25, GOT and Pt-Cu/P25 catalysts.

4.2 Photocatalytic Reduction of CO_2

The photocatalytic activity of P25 and the synthesized GOT and Pt-Cu/P25 composite materials for CO_2 reduction was examined in water under near-UV/Vis light irradiation. Products were not formed in blank tests conducted without photocatalysts under UV/Vis irradiation or with catalysts in the dark, indicating that the conversion is a photocatalytic reduction process that requires both photocatalysts and UV/Vis irradiation.

In the photocatalytic process, methanol and ethanol were the two major products that have been identified and quantified in this work. It is important to refer that it was not possible to trace the evolution of the products formation as a function of time by using the available GC-FID equipment. These products continuously accumulate in the reactor, but their amount

was above the quantification limit (for methanol and ethanol) only by the end of the experiments. Thus, all the obtained data are reported for a reaction time of 3 h. In addition, it was not possible to unravel the underlying reaction mechanism, since the identification and quantification of other possible reaction by-products was not possible probably because they are formed in lower amounts. This task should be conducted in future work and will be only possible by acquiring a new equipment with higher sensibility for analysis of these compounds.

Thus, the effect of initial pH on the photocatalytic efficiency for the formation of both methanol and ethanol (μmol g^{-1} h^{-1}, where g refers to the amount of catalyst) was studied by using three different initial pH values (3, 7 and 13). The results are shown in **Figures 26 a)** and **26 b),** respectively for P25 and GOT photocatalysts.

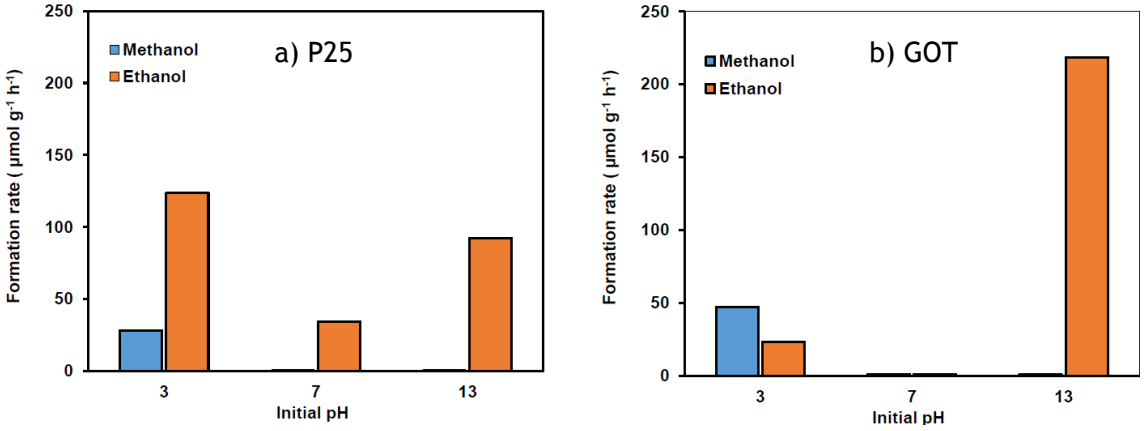

Figure 26- Photocatalytic reduction of CO_2 at different initial pH for a) P25 and b) GOT.

According to **Figure 26**, P25 exhibited superior performance at pH 3, for both methanol (28 μmol g^{-1} h^{-1}) and ethanol (123 μmol g^{-1} h^{-1}) formation, while GOT yielded highest ethanol formation rate (219 μmol g^{-1} h^{-1}) at initial pH 13 and the highest methanol formation rate (47 μmol g^{-1} h^{-1}) at pH 3. Therefore, the optimal pH seems to be related with the specific catalyst that is employed in this reaction and also with the target product, rather than with the sole effect of the CO_2 amount dissolved into the liquid (increasing with the solution pH). The works reported by Asi et al. [71] and Zhang et al. [70] referred an optimal pH 8.5 with an AgBr/TiO_2 catalyst (**Figure 16**) and pH 7 with a graphene-TiO_2 catalyst (**Figure 15**), respectively, regarding the highest yield for methanol formation. However, in the case of the graphene-TiO_2 composite, the results shown in the literature are quite similar at pH 4 and pH 7 (**Figure 15**). Thus, overall, it seems that the process performance strongly depends on the photocatalyst tested and also on the other conditions applied to conduct the reaction.

Regarding the results obtained at neutral pH (**Figure 26**), there is no excess of H^+ neither OH^-, thus $\dot{H}$ and $O\dot{H}$ are not so frequent, in this way decreasing the probability of their involvement in the target reactions for the significant formation of methanol and/or ethanol.

In what concerns the GOT catalyst at alkaline conditions as well as the P25 catalyst when applied at both acidic and alkaline conditions, one possible mechanism leading to the major formation of ethanol, in detriment of methanol, is the radical coupling reaction between $\dot{C}H_3$ and $H\dot{C}=O$, resulting in $CH_3HC=O$, which can be then reduced by hydrogen to form ethanol. A different predominant mechanism should be involved when GOT is applied at acidic conditions (pH 3), since methanol formation was slightly higher than that of ethanol for this particular experiment.

The point of zero charge (PZC) of the employed catalysts (ca. 3.0 for GOT [102] and 6.3 for P25 [116]) can also play a role in the process. The surface of both catalysts is negatively charged at a solution pH ≥ 7, while negatively charged carbon species are the prevalent form in solution in these conditions (HCO_3^- and/or CO_3^{2-}, as shown in **Figure 14**), these species being repulsed by the catalyst surface. Methanol was not formed at these neutral/alkaline conditions, regardless of the catalyst employed. At pH 3, H_2CO_3 is the predominant carbon species. Under these conditions, the GOT surface is uncharged and the P25 surface is positively charged. Even if the dissolved CO_2 levels in water are lower in acidic conditions (than in alkaline conditions), methanol was formed in this case, maybe because H^+ ions are abundant at these conditions (cf. **equation 8**).

Figure 27 shows the results obtained with the metallic co-catalyst (Pt-Cu/P25), and the respective reference material (P25), at pH 13. It is clear that the addition of platinum and copper metals to P25 significantly increases the photoactivity towards both methanol (18 μmol g^{-1} h^{-1}) and ethanol (167 μmol g^{-1} h^{-1}) formation yield.

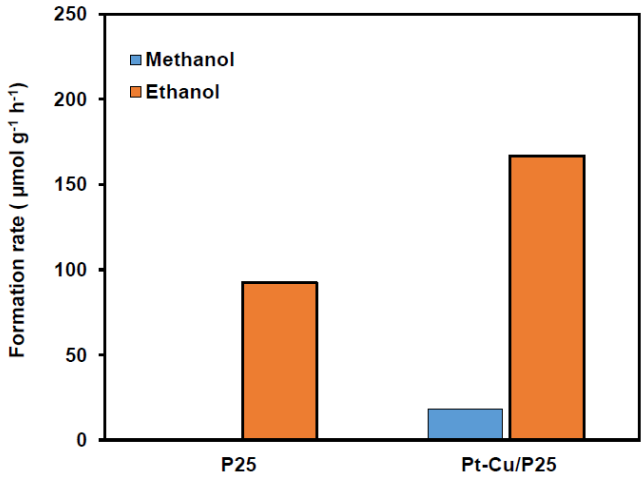

Figure 27- CO_2 photoreduction over P25 and Pt-Cu/P25 at initial pH 13.

It has been reported that an effective charge separation/transfer is crucial to enhance the photocatalytic activity [117]. The presence of a metal at the surface of P25 would result in the formation of a Schottky barrier at the metal–semiconductor interface. As the Fermi energy level of both Pt and Cu metals were lower than that of TiO_2, photoexcited electrons could be transferred from the CB to the metal particles, while the photogenerated holes remained on TiO_2 (VB) [117]. Therefore, the photocatalytic activity could be improved in terms of a longer electron–hole pair separation lifetime. Furthermore, the extended photoresponse range of the Pt-Cu/P25 catalyst (**Figure 25**) is also expected as positive contribution on the photocatalytic activity. Experiments with Pt-Cu/P25 at lower pH values, as well as with the other catalyst prepared (Pt-Cu/GOT) were also performed. However, the liquid samples were not analyzed due to technical limitations occurring with the gas chromatograph. Thus, the catalysts were properly stored and should be tested in future work.

Among the results obtained, the highest photocatalytic activity was obtained with the GOT composite, for ethanol formation at pH 13 and for methanol formation at pH 3. It has been suggested that the combination of TiO_2 with GO generates a synergistic effect that potentially enhances the photoactivity due to the possible improvements in the adsorption capacity and efficient interfacial electron transfer between the two constituent phases. In fact, a good assembly and interfacial coupling between the GO sheets and TiO_2 nanoparticles can be observed in the SEM micrograph of this composite (**Figure 23a**). Moreover, when GO is used to prepare the GOT composite it was proved that GO functionalities (such as epoxy and hydroxyl groups) mediate the efficient and uniform assembly of the TiO_2 nanoparticles on the GO sheets, leading to highly efficient photocatalysts when tested for the degradation of organic pollutants in aqueous solutions [118].

As the main product of the CO_2 photocatalytic reduction experiments (i.e. ethanol), it would be interesting to compare the highest ethanol formation rate (219 μmol g^{-1} h^{-1}) obtained with the GOT catalyst, at pH 13, with the literature discussed in the state of the art section. The highest ethanol formation rate reported by Abou et al. [42] was approximately 4 μmol g^{-1} h^{1} by using a Ag@ AgBr/CNT catalyst, as depicted in **Figure 7**. In this case, ethanol was a minor product, thus its formation rate was extremely lower (55 fold) than that obtained by using GOT, at initial pH 13. An ethanol formation rate of 3.6 μmol g^{-1} h^{-1} and 4.51 μmol g^{-1} h^{-1} was obtained by Mao et al. [63], by using a melamine derived g-C_3N_4 and a urea derived g-C_3N_4, respectively. As depicted in **Table 5,** ethanol was the second main product (following methanol), by using the urea-derived catalyst. When the melamine precursor was utilized, ethanol was the sole formed product. Once again, its formation rates are far away from that obtained with the GOT composite. It is interesting to note that in that case, supercritical CO_2 was flown into the reactor and the double of the power was used to irradiate the solution.

In another works, ethanol formation was also reported. Xia et al. [119] obtained an ethanol yield of 30 μmol g^{-1} h^{-1}, by using a TiO_2-MWCNT catalyst, in a gas phase reaction, with a 15 W UV lamp (365 nm). The other reported product was formic acid (19 μmol g^{-1} h^{-1}). Later, Liu et al. [120] reported an ethanol production rate of 110 μmol g^{-1} h^{-1}, by using a monoclinic $BiVO_4$ photocatalyst, suspended in 100 mL of water and irradiated by a 300 W Xe lamp emitting in the visible part of the spectrum. The authors suggested that intense irradiation generates a large number of C1 intermediate species anchored on the surface of $BiVO_4$, which dimerizes to form ethanol. This was just a supposition and more studies are required to clarify the ethanol formation mechanism.

5 Conclusions

The photocatalytic reduction of CO_2 is deemed as an excellent solution to the global warming and energy crisis. Unfortunately, it is clear that this solar technology is not yet ready to be implemented in commercial solar fuel applications. There is an imperative necessity to (i) develop highly efficient, selective and stable photocatalysts; (ii) study the influence of the reaction conditions on solar fuel production and (iii) determine the surface species intermediates and reaction pathways to the formation of the selected fuels.

To improve the efficiency of photocatalysts, different carbonaceous materials, such as CNTs, graphene and its derivatives as well as g-C_3N_4 have been used to produce carbon-based composites constituting an exciting approach for the design of superior novel materials due to their unique properties improving the adsorption of reactants and intermediate species, the electron-hole separation capacity and the enhanced photocatalytic activity.

As reviewed in the state of the art, the both methanol and methane formation rates were enhanced by the combination of CNT with photocatalysts, such as TiO_2 and AgBr. Similarly, methanol, carbon monoxide and methane yields were increased after the incorporation of graphene derivatives in bare semiconductors, like TiO_2, Cu_2O and ZnO. The g-C_3N_4 based photocatalysts have also demonstrated an enormous potential in this field either by bare application or by combination with WO_3, ZnO and Ag_3PO_4.

Co-metals are important to maximize yield rates. The metal nanoparticles could help to improve recombination times of charge carriers as well as increase the absorption band in the visible region. In this context, some modification strategies, targeting improved solar fuel yields, have also arisen, with noble metal loading such as Cu and Pt.

The effectiveness and product selectivity of photocatalytic reactions is achieved by selecting an appropriate reductant. Water is seen as the supreme reducing agent, but it can compete advantageously with CO_2 for electrons in the semiconductor CB, constituting an enormous drawback in the photocatalytic reduction of CO_2. To overcome the limitations of using water as reducing agent, other electron donors, such as sodium hydroxide, sodium sulphite, isopropyl alcohol, hydrogen and monoethanolamine have been applied with increased solar fuel production. Furthermore, it was shown that the initial solution pH is a vital parameter to CO_2 reduction, because the process is affected by the carbon species in the solution. According to the literature, the neutral and weak alkaline conditions were desirable. In the

present dissertation, GO-TiO_2 composites and Pt-Cu/P25 bimetallic catalysts have been prepared and characterized to be used for the CO_2 photoreduction to hydrocarbons in water, at different initial solution pH. The photocatalytic activity of a Pt-Cu/P25 bimetallic catalyst exceeded that of the benchmark P25 photocatalyst for the photoreduction of CO_2 to both methanol and ethanol at pH 13. This indicates that the presence of metals may effectively improve the photocatalyt activity, due to both longer electron–hole pair separation lifetime as well as the extended photoresponse range of the Pt-Cu/P25 catalyst. Among all the prepared catalysts, GOT was the best performing material for both methanol and ethanol production at the initial solution pH of 3 and 13, respectively. This superior performance was attributed to the synergetic interaction encompassing both interfacial electron transfer between the two constituent phases as well as to the higher BET surface area, improving the adsorption of reactants.

It is worth noting that the ethanol formation rate is really high when compared to the others found in literature. Nevertheless, the formation rate of a solar fuel is a misleading parameter, as it does not include the moles of CO_2 involved in the reaction; the light power (and spectrum); or even the activity decay over time. All these parameters should be included to measure the photocatalyst efficiency and to authentically compare the performance of different photocatalysts under such heterogeneous reaction conditions. Furthermore, the irradiation conditions should be standardized, as already happens in the photovoltaic industry.

6 Future Work

As previously mentioned, the development of the experimental part of this dissertation was compromised in some extent by the available GC-FID equipment, due to the impossibility for determining the product amounts below the quantification limit (ca. 0.05 mM). Nevertheless, the problem is expected to be solved in a near future, and the following possible studies are proposed:

- To perform experiments with the samples that were prepared, characterized and stored but that were not tested in the present dissertation;
- To analyze the effect of isopropyl alcohol and other electron donors;
- To perform the photocatalytic experiments using different buffer solutions;
- To prepare photocatalysts with the same metallic elements and CNTs as well as g-C_3N_4 based materials;
- To increase the reaction time in order to have a better understanding of the evolution of the products over time;
- To use different light sources, such as light-emitting diodes (LEDs);
- To reuse the photocatalysts in consecutive runs and evaluate their stability;
- To fabricate a lab-scale set-up for photocatalytic conversion of CO_2 in gas-solid conditions.

References

1. VijayaVenkataRaman, S., Iniyan, S. and Goic, R. (2012). A review of climate change, mitigation and adaptation. *Renewable and Sustainable Energy Reviews*, 16(1), pp.878-897.
2. Riebeek, H. (2010). *Global Warming : Feature Articles*. [online] Earthobservatory.nasa.gov. Available at: http://earthobservatory.nasa.gov/Features/GlobalWarming. [Accessed 25 Mar. 2015].
3. Kalogirou, S. ed., (2009). Chapter two - Environmental Characteristics,. In: *Solar Energy Engineering*, 1st ed. Boston: Academic Press.
4. Elder, W. (2015). *What is Climate Change? - Great Basin National Park (U.S. National Park Service)*. [online] Nps.gov. Available at: http://www.nps.gov/grba/learn/nature/what-is-climate-change.htm [Accessed 26 Mar. 2015].
5. Cdiac.ornl.gov, (2015). *Current Greenhouse Gas Concentrations*. [online] Available at: http://cdiac.ornl.gov/pns/current_ghg.html [Accessed 28 Mar. 2015].
6. Xu, and Moulijn, J. (1996). Mitigation of CO_2 by Chemical Conversion: Plausible Chemical Reactions and Promising Products. *Energy Fuels*, 10(2), pp.305-325.
7. Scripps Institution of Oceanography, (2015). *The Keeling Curve*. [online] Available at: https://scripps.ucsd.edu/programs/keelingcurve/wp-content/plugins/sio-bluemoon/graphs/co2_800k.png [Accessed 3 May 2015].
8. PBL Netherland Environmental Assessment Agency, (2014). *Trends in Global CO_2 emissions: 2014 Report*. [online] The Hague: PBL and Joint Research Centre. Available at: http://edgar.jrc.ec.europa.eu/news_docs/jrc-2014-trends-in-global-co2-emissions-2014-report-93171.pdf [Accessed 22 Apr. 2015].
9. Tahir, M. and Amin, N. (2013). Recycling of carbon dioxide to renewable fuels by photocatalysis: Prospects and challenges. *Renewable and Sustainable Energy Reviews*, 25, pp.560-579.
10. Cuéllar-Franca, R. and Azapagic, A. (2015). Carbon capture, storage and utilisation technologies: A critical analysis and comparison of their life cycle environmental impacts. *Journal of CO_2 Utilization*, 9, pp.82-102.
11. Pasten, C. and Santamarina, J. (2012). Energy and quality of life. *Energy Policy*, 49, pp.468-476.
12. British Petroleum, (2014). *Statistical Review of World Energy June 2014*. [online] London: BP Statistical Review of World Energy, pp.40-42. Available at: http://www.bp.com/content/dam/bp/pdf/Energy-economics/statistical-review-2014/BP-statistical-review-of-world-energy-2014-full-report.pdf [Accessed 10 Apr. 2015].
13. International Energy Agency and Nuclear Energy Agency, (2015). *Nuclear Energy*. Technology Roadmap. [online] Paris: International Energy Agency. Available at: https://www.iea.org/media/freepublications/technologyroadmaps/TechnologyRoadmapNuclearEnergy.pdf [Accessed 18 Mar. 2015].
14. Centi, G. and Perathoner, S. (2010). Towards Solar Fuels from Water and CO_2. *CHEMSUSCHEM*, 3(2), pp.195-208.
15. Das, S. and Wan Daud, W. (2014). Photocatalytic CO_2 transformation into fuel: A review on advances in photocatalyst and photoreactor. *Renewable and Sustainable Energy Reviews*, 39, pp.765-805.

16. Panwar, N., Kaushik, S. and Kothari, S. (2011). Role of renewable energy sources in environmental protection: A review. *Renewable and Sustainable Energy Reviews*, 15(3), pp.1513-1524.
17. Kalogirou, S. ed., (2009). Chapter one - Introduction. In: *Solar Energy Engineering*, 1st ed. Boston: Academic Press.
18. Habisreutinger, S., Schmidt-Mende, L. and Stolarczyk, J. (2013). Photocatalytic Reduction of CO_2 on TiO_2 and Other Semiconductors. *Angew. Chem. Int. Ed.*, 52(29), pp.7372-7408.
19. Gust, D., Moore, T. and Moore, A. (2009). Solar Fuels via Artificial Photosynthesis. *Acc. Chem. Res.*, 42(12), pp.1890-1898.
20. Ganesh, I. (2014). Conversion of carbon dioxide into methanol – a potential liquid fuel: Fundamental challenges and opportunities (a review). *Renewable and Sustainable Energy Reviews*, 31, pp.221-257.
21. Tu, W., Zhou, Y. and Zou, Z. (2014). Photoconversion: Photocatalytic Conversion of CO_2 into Renewable Hydrocarbon Fuels: State-of-the-Art Accomplishment, Challenges, and Prospects (Adv. Mater. 27/2014). *Adv. Mater.*, 26(27), pp.4598-4598.
22. Ahmad, H., Kamarudin, S., Minggu, L. and Kassim, M. (2015). Hydrogen from photo-catalytic water splitting process: A review. *Renewable and Sustainable Energy Reviews*, 43, pp.599-610.
23. Herron, J., Kim, J., Upadhye, A., Huber, G. and Maravelias, C. (2015). A general framework for the assessment of solar fuel technologies. *Energy Environ. Sci.*, 8(1), pp.126-157.
24. Xiao, L., Wu, S. and Li, Y. (2012). Advances in solar hydrogen production via two-step water-splitting thermochemical cycles based on metal redox reactions. *Renewable Energy*, 41, pp.1-12.
25. Ma, J., Sun, N., Zhang, X., Zhao, N., Xiao, F., Wei, W. and Sun, Y. (2009). A short review of catalysis for CO_2 conversion. *Catalysis Today*, 148(3-4), pp.221-231.
26. Gupta, S. and Tripathi, M. (2011). An overview of commonly used semiconductor nanoparticles in photocatalysis. *High Energy Chem*, 46(1), pp.1-9.
27. Herrmann, J. (2005). Heterogeneous photocatalysis: state of the art and present applications. *Topics in Catalysis*, 34(1-4), pp.49-65.
28. Mikkelsen, M., Jørgensen, M. and Krebs, F. (2010). The teraton challenge. A review of fixation and transformation of carbon dioxide. *Energy Environ. Sci.*, 3(1), pp.43-81.
29. Ma, Y., Wang, X., Jia, Y., Chen, X., Han, H. and Li, C. (2014). Titanium Dioxide-Based Nanomaterials for Photocatalytic Fuel Generations. *Chem. Rev.*, 114(19), pp.9987-10043.
30. Benson, E., Kubiak, C., Sathrum, A. and Smieja, J. (2009). Electrocatalytic and homogeneous approaches to conversion of CO_2 to liquid fuels. *Chem. Soc. Rev.*, 38(1), pp.89-99.
31. Indrakanti, V., Kubicki, J. and Schobert, H. (2009). Photoinduced activation of CO_2 on Ti-based heterogeneous catalysts: Current state, chemical physics-based insights and outlook. *Energy Environ. Sci.*, 2(7), pp.745-758.
32. Schneider, J., Jia, H., Muckerman, J. and Fujita, E. (2012). Thermodynamics and kinetics of CO_2, CO, and H+ binding to the metal centre of CO_2 reductioncatalysts. *Chem. Soc. Rev.*, 41(6), pp.2036-2051.
33. Wang, W. (2014). Comparison of CO_2 Photoreduction Systems: A Review. *Aerosol and Air Quality Research*.
34. Tahir, M. and Amin, N. (2013). Advances in visible light responsive titanium oxide-based photocatalysts for CO_2 conversion to hydrocarbon fuels. *Energy Conversion and Management*, 76, pp.194-214.

35. Inoue, T., Fujishima, A., Konishi, S. and Honda, K. (1979). Photoelectrocatalytic reduction of carbon dioxide in aqueous suspensions of semiconductor powders. *Nature*, 277(5698), pp.637-638.
36. Saleh, T. (2013). The Role of Carbon Nanotubes in Enhancement of Photocatalysis. In: *Syntheses and Applications of Carbon Nanotubes and Their Composites*, 1st ed. [online] Available at: http://cdn.intechopen.com/pdfs-wm/38214.pdf [Accessed 7 Jun. 2015].
37. Serp, P. and Figueiredo, J. (2009). *Carbon materials for catalysis*. Hoboken, N.J.: John Wiley & Sons, pp.309-312.
38. Iijima, S. (1991). Helical microtubules of graphitic carbon. *Nature*, 354(6348), pp.56-58.
39. Leary, R. and Westwood, A. (2011). Carbonaceous nanomaterials for the enhancement of TiO_2 photocatalysis. *Carbon*, 49(3), pp.741-772.
40. Sun, H. and Wang, S. (2014). Research Advances in the Synthesis of Nanocarbon-Based Photocatalysts and Their Applications for Photocatalytic Conversion of Carbon Dioxide to Hydrocarbon Fuels. *Energy Fuels*, 28(1), pp.22-36.
41. Gui, M., Chai, S. and Mohamed, A. (2014). Modification of MWCNT@TiO_2 core–shell nanocomposites with transition metal oxide dopants for photoreduction of carbon dioxide into methane. *Applied Surface Science*, 319, pp.37-43.
42. Abou Asi, M., Zhu, L., He, C., Sharma, V., Shu, D., Li, S., Yang, J. and Xiong, Y. (2013). Visible-light-harvesting reduction of CO_2 to chemical fuels with plasmonic Ag@AgBr/CNT nanocomposites. *Catalysis Today*, 216, pp.268-275.
43. Gui, M., Chai, S., Xu, B. and Mohamed, A. (2014). Enhanced visible light responsive MWCNT/TiO_2 core–shell nanocomposites as the potential photocatalyst for reduction of CO_2 into methane. *Solar Energy Materials and Solar Cells*, 122, pp.183-189.
44. Taheri Najafabadi, A. (2015). Emerging applications of graphene and its derivatives in carbon capture and conversion: Current status and future prospects. *Renewable and Sustainable Energy Reviews*, 41, pp.1515-1545.
45. Tu, W., Zhou, Y. and Zou, Z. (2013). Versatile Graphene-Promoting Photocatalytic Performance of Semiconductors: Basic Principles, Synthesis, Solar Energy Conversion, and Environmental Applications. *Advanced Functional Materials*, 23(40), pp.4996-5008..
46. Singh, V., Joung, D., Zhai, L., Das, S., Khondaker, S. and Seal, S. (2011). Graphene based materials: Past, present and future. *Progress in Materials Science*, 56(8), pp.1178-1271.
47. Pei, S. and Cheng, H. (2012). The reduction of graphene oxide. *Carbon*, 50(9), pp.3210-3228.
48. Kim, J., Hwang, J., Suh, J., Tongay, S., Kwon, S., Hwang, C., Wu, J. and Young Park, J. (2013). Work function engineering of single layer graphene by irradiation-induced defects. *Applied Physics Letters*, 103(17), p.171604.
49. Williams, G., Seger, B. and Kamat, P. (2008). TiO_2-Graphene Nanocomposites. UV-Assisted Photocatalytic Reduction of Graphene Oxide. *ACS Nano*, 2(7), pp.1487-1491.
50. Tan, L., Ong, W., Chai, S. and Mohamed, A. (2015). Noble metal modified reduced graphene oxide/TiO_2 ternary nanostructures for efficient visible-light-driven photoreduction of carbon dioxide into methane. *Applied Catalysis B: Environmental*, 166-167, pp.251-259.
51. An, X., Li, K. and Tang, J. (2014). Cu_2O/Reduced Graphene Oxide Composites for the Photocatalytic Conversion of CO_2. *CHEMSUSCHEM*, 7(4), pp.1086-1093.
52. Wang, A., Li, X., Zhao, Y., Wu, W., Chen, J. and Meng, H. (2014). Preparation and characterizations of Cu_2O/reduced graphene oxide nanocomposites with high photo-catalytic performances. *Powder Technology*, 261, pp.42-48.

53. Shown, I., Hsu, H., Chang, Y., Lin, C., Roy, P., Ganguly, A., Wang, C., Chang, J., Wu, C., Chen, L. and Chen, K. (2014). Highly Efficient Visible Light Photocatalytic Reduction of CO_2 to Hydrocarbon Fuels by Cu-Nanoparticle Decorated Graphene Oxide. *Nano Letters*, 14(11), pp.6097-6103.
54. Li, X., Wang, Q., Zhao, Y., Wu, W., Chen, J. and Meng, H. (2013). Green synthesis and photo-catalytic performances for ZnO-reduced graphene oxide nanocomposites. *Journal of Colloid and Interface Science*, 411, pp.69-75.
55. An, X., Li, K. and Tang, J. (2014). Cu_2O/Reduced Graphene Oxide Composites for the Photocatalytic Conversion of CO_2. *CHEMSUSCHEM*, 7(4), pp.1086-1093.
56. Thomas, A., Fischer, A., Goettmann, F., Antonietti, M., Müller, J., Schlögl, R. and Carlsson, J. (2008). Graphitic carbon nitride materials: variation of structure and morphology and their use as metal-free catalysts. *Journal of Materials Chemistry*, 18(41), po.4893-4908.
57. Wang, K., Li, Q., Liu, B., Cheng, B., Ho, W. and Yu, J. (2015). Sulfur-doped g-C_3N_4 with enhanced photocatalytic CO_2-reduction performance. *Applied Catalysis B: Environmental*, 176-177, pp.44-52.
58. Zhu, J., Xiao, P., Li, H. and Carabineiro, S. (2014). Graphitic Carbon Nitride: Synthesis, Properties, and Applications in Catalysis. *ACS Appl. Mater. Interfaces*, 6(19), pp.16449-16465.
59. Ohno, T., Murakami, N., Koyanagi, T. and Yang, Y. (2014). Photocatalytic reduction of CO_2 over a hybrid photocatalyst composed of WO_3 and graphitic carbon nitride (g-C_3N_4) under visible light. *Journal of CO_2 Utilization*, 6, pp.17-25.
60. Yu, J., Wang, K., Xiao, W. and Cheng, B. (2014). Photocatalytic reduction of CO2 into hydrocarbon solar fuels over g-C_3N_4–Pt nanocomposite photocatalysts. *Phys. Chem. Chem. Phys.*, 16(23), pp.11492-11501.
61. Wang, X., Maeda, K., Thomas, A., Takanabe, K., Xin, G., Carlsson, J., Domen, K. and Antonietti, M. (2008). A metal-free polymeric photocatalyst for hydrogen production from water under visible light. *Nat Mater*, 8(1), pp.76-80.
62. Niu, P., Yang, Y., Yu, J., Liu, G. and Cheng, H. (2014). Switching the selectivity of the photoreduction reaction of carbon dioxide by controlling the band structure of a g-C_3N_4 photocatalyst. *Chem. Commun.*, 50(74), pp.10837-10840.
63. Mao, J., Peng, T., Zhang, X., Li, K., Ye, L. and Zan, L. (2013). Effect of graphitic carbon nitride microstructures on the activity and selectivity of photocatalytic CO_2 reduction under visible light. *Catal. Sci. Technol.*, 3(5), pp.1253-1260.
64. Ong, W., Tan, L., Chai, S. and Yong, S. (2015). Heterojunction engineering of graphitic carbon nitride (g-C_3N_4) via Pt loading with improved daylight-induced photocatalytic reduction of carbon dioxide to methane. *Dalton Trans.*, 44(3), pp.1249-1257.
65. He, Y., Wang, Y., Zhang, L., Teng, B. and Fan, M. (2015). High-efficiency conversion of CO_2 to fuel over ZnO/g-C_3N_4 photocatalyst. *Applied Catalysis B: Environmental*, 168-169, pp.1-8.
66. He, Y., Zhang, L., Teng, B. and Fan, M. (2015). New Application of Z-Scheme Ag_3PO_4/g-C_3N_4 Composite in Converting CO_2 to Fuel. *Environmental Science & Technology*, 49(1), pp.649-656.
67. Corma, A. and Garcia, H. (2013). Photocatalytic reduction of CO_2 for fuel production: Possibilities and challenges. *Journal of Catalysis*, 308, pp.168-175.
68. Neațu, Ș., Maciá-Agulló, J. and Garcia, H. (2014). Solar Light Photocatalytic CO_2 Reduction: General Considerations and Selected Bench-Mark Photocatalysts. *IJMS*, 15(4), pp.5246-5262.
69. Zasoski, (2002). *Carbonate Chemistry*. 1st ed. [ebook] Available at: http://lawr.ucdavis.edu/classes/ssc102/Section5.pdf [Accessed 14 May 2015].

70. Zhang, Q., Lin, C., Chen, B., Ouyang, T. and Chang, C. (2015). Deciphering Visible Light Photoreductive Conversion of CO_2 to Formic Acid and Methanol Using Waste Prepared Material. *Environmental Science & Technology*, 49(4), pp.2405-2417.
71. Abou Asi, M., He, C., Su, M., Xia, D., Lin, L., Deng, H., Xiong, Y., Qiu, R. and Li, X. (2011). Photocatalytic reduction of CO_2 to hydrocarbons using $AgBr/TiO_2$ nanocomposites under visible light. *Catalysis Today*, 175(1), pp.256-263.
72. Mori, K., Yamashita, H. and Anpo, M. (2012). Photocatalytic reduction of CO_2 with H_2O on various titanium oxide photocatalysts. *RSC Advances*, 2(8), pp.3165-3172.
73. Liu, S., Zhao, Z. and Wang, Z. (2007). Photocatalytic reduction of carbon dioxide using sol-gel derived titania-supported CoPc catalysts. *Photochem. Photobiol. Sci.*, 6(6), pp.695-700.
74. Kočí, K., Obalová, L., Matějová, L., Plachá, D., Lacný, Z., Jirkovský, J. and Šolcová, O. (2009). Effect of TiO_2 particle size on the photocatalytic reduction of CO_2. *Applied Catalysis B: Environmental*, 89(3-4), pp.494-502.
75. Kočí, K., Matějová, L., Kozák, O., Čapek, L., Valeš, V., Reli, M., Praus, P., Šafářová, K., Kotarba, A. and Obalová, L. (2014). ZnS/MMT nanocomposites: The effect of ZnS loading in MMT on the photocatalytic reduction of carbon dioxide. *Applied Catalysis B: Environmental*, 158-159, pp.410-417.
76. Tseng, I., Wu, J. and Chou, H. (2004). Effects of sol–gel procedures on the photocatalysis of Cu/TiO_2 in CO_2 photoreduction. *Journal of Catalysis*, 221(2), pp.432-440.
77. Li, Q., Zong, L., Li, C. and Yang, J. (2014). Photocatalytic reduction of CO_2 on MgO/TiO_2 nanotube films. *Applied Surface Science*, 314, pp.458-463.
78. Liu, Q., Low, Z., Li, L., Razmjou, A., Wang, K., Yao, J. and Wang, H. (2013). ZIF-8/Zn_2GeO_4 nanorods with an enhanced CO_2 adsorption property in an aqueous medium for photocatalytic synthesis of liquid fuel. *Journal of Materials Chemistry A*, 1(38), pp.11563-11569.
79. Reli, M., Šihor, M., Kočí, K., Praus, P., Kozák, O. and Obalová, L. (2012). Influence of Reaction Medium on CO_2 Photocatalytic Reduction Yields Over Zns-MMT / Vliv Reakčního Prostření Na Výtěžky Fotokatalytické Redukce CO_2 V Přítomnosti Zns-MMT. *GeoScience Engineering*, 58(1), pp.34-42.
80. Sato, S., Morikawa, T., Saeki, S., Kajino, T. and Motohiro, T. (2010). Visible-Light-Induced Selective CO_2 Reduction Utilizing a Ruthenium Complex Electrocatalyst Linked to a p-Type Nitrogen-Doped Ta_2O_5 Semiconductor. *Angewandte Chemie*, 122(30), pp.5227-5231.
81. Suzuki, T., Tanaka, H., Morikawa, T., Iwaki, M., Sato, S., Saeki, S., Inoue, M., Kajino, T. and Motohiro, T. (2011). Direct assembly synthesis of metal complex–semiconductor hybrid photocatalysts anchored by phosphonate for highly efficient CO_2 reduction. *Chem. Commun.*, 47(30), pp.8673-8675.
82. Fu, Y., Sun, D., Chen, Y., Huang, R., Ding, Z., Fu, X. and Li, Z. (2012). An Amine-Functionalized Titanium Metal-Organic Framework Photocatalyst with Visible-Light-Induced Activity for CO_2 Reduction. *Angew. Chem.*, 124(14), pp.3420-3423.
83. Sun, D., Fu, Y., Liu, W., Ye, L., Wang, D., Yang, L., Fu, X. and Li, Z. (2013). Studies on Photocatalytic CO 2 Reduction over NH 2 -Uio-66(Zr) and Its Derivatives: Towards a Better Understanding of Photocatalysis on Metal-Organic Frameworks. *Chemistry - A European Journal*, 19(42), pp.14279-14285.
84. Fujiwara, H., Hosokawa, H., Murakoshi, K., Wada, Y., Yanagida, S., Okada, T. and Kobayashi, H. (1997). Effect of Surface Structures on Photocatalytic CO_2 Reduction Using Quantized CdS Nanocrystallites 1. *J. Phys. Chem. B*, 101(41), pp.8270-8278.

85. Wang, C., Xie, Z., deKrafft, K. and Lin, W. (2011). Doping Metal–Organic Frameworks for Water Oxidation, Carbon Dioxide Reduction, and Organic Photocatalysis. *J. Am. Chem. Soc.*, 133(34), pp.13445-13454.
86. Qin, S., Xin, F., Liu, Y., Yin, X. and Ma, W. (2011). Photocatalytic reduction of CO_2 in methanol to methyl formate over CuO–TiO_2 composite catalysts. *Journal of Colloid and Interface Science*, 356(1), pp.257-261.
87. Sekizawa, K., Maeda, K., Domen, K., Koike, K. and Ishitani, O. (2013). Artificial Z-Scheme Constructed with a Supramolecular Metal Complex and Semiconductor for the Photocatalytic Reduction of CO_2. *J. Am. Chem. Soc.*, 135(12), pp.4596-4599.
88. Sui, D., Yin, X., Dong, H., Qin, S., Chen, J. and Jiang, W. (2012). Photocatalytically Reducing CO_2 to Methyl Formate in Methanol Over Ag Loaded $SrTiO_3$ Nanocrystal Catalysts. *Catalysis Letters*, 142(10), pp.1202-1210.
89. Kaneco, S., Shimizu, Y., Ohta, K. and Mizuno, T. (1998). Photocatalytic reduction of high pressure carbon dioxide using TiO_2 powders with a positive hole scavenger. *Journal of Photochemistry and Photobiology A: Chemistry*, 115(3), pp.223-226.
90. Liu, B., Torimoto, T. and Yoneyama, H. (1998). Photocatalytic reduction of CO_2 using surface-modified CdS photocatalysts in organic solvents. *Journal of Photochemistry and Photobiology A: Chemistry*, 113(1), pp.93-97.
91. Kohno, Y., Tanaka, T., Funabiki, T. and Yoshida, S. (2000). Photoreduction of CO_2 with H_2 over ZrO_2. A study on interaction of hydrogen with photoexcited CO_2. *Phys. Chem. Chem. Phys.*, 2(11), pp.2635-2639..
92. Kohno, Y., Ishikawa, H., Tanaka, T., Funabiki, T. and Yoshida, S. (2001). Photoreduction of carbon dioxide by hydrogen over magnesium oxide. *Phys. Chem. Chem. Phys.*, 3(6), pp.1108-1113.
93. Teramura, K., Okuoka, S., Tsuneoka, H., Shishido, T. and Tanaka, T. (2010). Photocatalytic reduction of CO_2 using H_2 as reductant over $ATaO_3$ photocatalysts (A=Li, Na, K). *Applied Catalysis B: Environmental*, 96(3-4), pp.565-568.
94. Ahmed, N., Morikawa, M. and Izumi, Y. (2012). Photocatalytic conversion of carbon dioxide into methanol using optimized layered double hydroxide catalysts. *Catalysis Today*, 185(1), pp.263-269.
95. Aliwi, S. and Al-Jubori, K. (1989). Photoreduction of CO_2 by metal sulphide semiconductors in presence of H_2S. *Solar Energy Materials*, 18(3-4), pp.223-229.
96. Yoshida, H. and Maeda, K. (2010). Preparation of gallium oxide photocatalysts for reduction of carbon dioxide. *Studies in Surface Science and Catalysis*, 175, pp.351-354.
97. Yuliati, L., Itoh, H. and Yoshida, H. (2008). Photocatalytic conversion of methane and carbon dioxide over gallium oxide. *Chemical Physics Letters*, 452(1-3), pp.178-182.
98. Wu, H., Bai, H. and Wu, J. (2014). Photocatalytic Reduction of CO_2 Using Ti–MCM-41 Photocatalysts in Monoethanolamine Solution for Methane Production. *Industrial & Engineering Chemistry Research*, 53(28), pp.11221-11227.
99. Hummers, W. and Offeman, R. (1958). Preparation of Graphitic Oxide. *J. Am. Chem. Soc.*, 80(6), pp.1339-1339.
100. Stankovich, S., Dikin, D., Piner, R., Kohlhaas, K., Kleinhammes, A., Jia, Y., Wu, Y., Nguyen, S. and Ruoff, R. (2007). Synthesis of graphene-based nanosheets via chemical reduction of exfoliated graphite oxide. *Carbon*, 45(7), pp.1558-1565..

101. Pastrana-Martínez, L., Morales-Torres, S., Likodimos, V., Figueiredo, J., Faria, J., Falaras, P. and Silva, A. (2012). Advanced nanostructured photocatalysts based on reduced graphene oxide–TiO_2 composites for degradation of diphenhydramine pharmaceutical and methyl orange dye. *Applied Catalysis B: Environmental*, 123-124, pp.241-256.
102. Pastrana-Martínez, L., Morales-Torres, S., Papageorgiou, S., Katsaros, F., Romanos, G., Figueiredo, J., Faria, J., Falaras, P. and Silva, A. (2013). Photocatalytic behaviour of nanocarbon–TiO_2 composites and immobilization into hollow fibres. *Applied Catalysis B: Environmental*, 142-143, pp.101-111.
103. Pastrana-Martínez, L., Morales-Torres, S., Carabineiro, S., Buijnsters, J., Faria, J., Figueiredo, J. and Silva, A. (2013). Nanodiamond-TiO_2 Composites for Heterogeneous Photocatalysis. *CHEMPLUSCHEM*, 78(8), pp.801-807.
104. Brunauer, S., Emmett, P. and Teller, E. (1938). Adsorption of Gases in Multimolecular Layers. *J. Am. Chem. Soc.*, 60(2), pp.309-319.
105. Delannoy, L., Thrimurthulu, G., Reddy, P., Méthivier, C., Nelayah, J., Reddy, B., Ricolleau, C. and Louis, C. (2014). Selective hydrogenation of butadiene over TiO_2 supported copper, gold and gold–copper catalysts prepared by deposition–precipitation. *Phys. Chem. Chem. Phys.*, 16(48), pp.26514-26527.
106. Ou, T., Chang, F. and Roselin, L. (2008). Production of hydrogen via partial oxidation of methanol over bimetallic Au–Cu/TiO_2 catalysts. *Journal of Molecular Catalysis A: Chemical*, 293(1-2), pp.8-16.
107. Cárdenas-Lizana, F., Gómez-Quero, S., Hugon, A., Delannoy, L., Louis, C. and Keane, M. (2009). Pd-promoted selective gas phase hydrogenation of p-chloronitrobenzene over alumina supported Au. *Journal of Catalysis*, 262(2), pp.235-243.
108. Pastrana-Martínez, L., Morales-Torres, S., Likodimos, V., Figueiredo, J., Faria, J., Falaras, P. and Silva, A. (2012). Advanced nanostructured photocatalysts based on reduced graphene oxide–TiO_2 composites for degradation of diphenhydramine pharmaceutical and methyl orange dye. *Applied Catalysis B: Environmental*, 123-124, pp.241-256.
109. Maira, A., Coronado, J., Augugliaro, V., Yeung, K., Conesa, J. and Soria, J. (2001). Fourier Transform Infrared Study of the Performance of Nanostructured TiO_2 Particles for the Photocatalytic Oxidation of Gaseous Toluene. *Journal of Catalysis*, 202(2), pp.413-420.
110. Martra, G. (2000). Lewis acid and base sites at the surface of microcrystalline TiO_2 anatase: relationships between surface morphology and chemical behaviour. *Applied Catalysis A: General*, 200(1-2), pp.275-285.
111. Yudianti, R. (2011). Analysis of Functional Group Sited on Multi-Wall Carbon Nanotube Surface. *The Open Materials Science Journal*, 5(1), pp.242-247.
112. Morales-Torres, S., Pastrana-Martínez, L., Figueiredo, J., Faria, J. and Silva, A. (2012). Design of graphene-based TiO_2 photocatalysts—a review. *Environ Sci Pollut Res*, 19(9), pp.3676-3687.
113. Silva, C. and Faria, J. (2010). Photocatalytic oxidation of benzene derivatives in aqueous suspensions: Synergic effect induced by the introduction of carbon nanotubes in a TiO_2 matrix. *Applied Catalysis B: Environmental*, 101(1-2), pp.81-89.
114. Lim, H., Park, S., Cheong, H., Choi, H. and Kim, Y. (2006). Photoluminescence of natural diamonds. *Journal-Korean Physical Society*, 48(6), p.1556.
115. Wang, C., Chen, Z., Jin, H., Cao, C., Li, J. and Mi, Z. (2014). Enhancing visible-light photoelectrochemical water splitting through transition-metal doped TiO_2 nanorod arrays. *J. Mater. Chem. A*, 2(42), pp.17820-17827.

116. Pastrana-Martínez, L., Faria, J., Doña-Rodríguez, J., Fernández-Rodríguez, C. and Silva, A. (2012). Degradation of diphenhydramine pharmaceutical in aqueous solutions by using two highly active TiO_2 photocatalysts: Operating parameters and photocatalytic mechanism. *Applied Catalysis B: Environmental*, 113-114, pp.221-227.
117. Zhai, Q., Xie, S., Fan, W., Zhang, Q., Wang, Y., Deng, W. and Wang, Y. (2013). Photocatalytic Conversion of Carbon Dioxide with Water into Methane: Platinum and Copper(I) Oxide Co-catalysts with a Core-Shell Structure. *Angew. Chem.*, 125(22), pp.5888-5891.
118. Pastrana-Martínez, L., Morales-Torres, S., Likodimos, V., Falaras, P., Figueiredo, J., Faria, J. and Silva, A. (2014). Role of oxygen functionalities on the synthesis of photocatalytically active graphene–TiO_2 composites. *Applied Catalysis B: Environmental*, 158-159, pp.329-340.
119. Xia, X., Jia, Z., Yu, Y., Liang, Y., Wang, Z. and Ma, L. (2007). Preparation of multi-walled carbon nanotube supported TiO_2 and its photocatalytic activity in the reduction of CO_2 with H_2O. *Carbon*, 45(4), pp.717-721.
120. Liu, Y., Huang, B., Dai, Y., Zhang, X., Qin, X., Jiang, M. and Whangbo, M. (2009). Selective ethanol formation from photocatalytic reduction of carbon dioxide in water with $BiVO_4$ photocatalyst. *Catalysis Communications*, 11(3), pp.210-213.

Appendix A: Calibration Curves

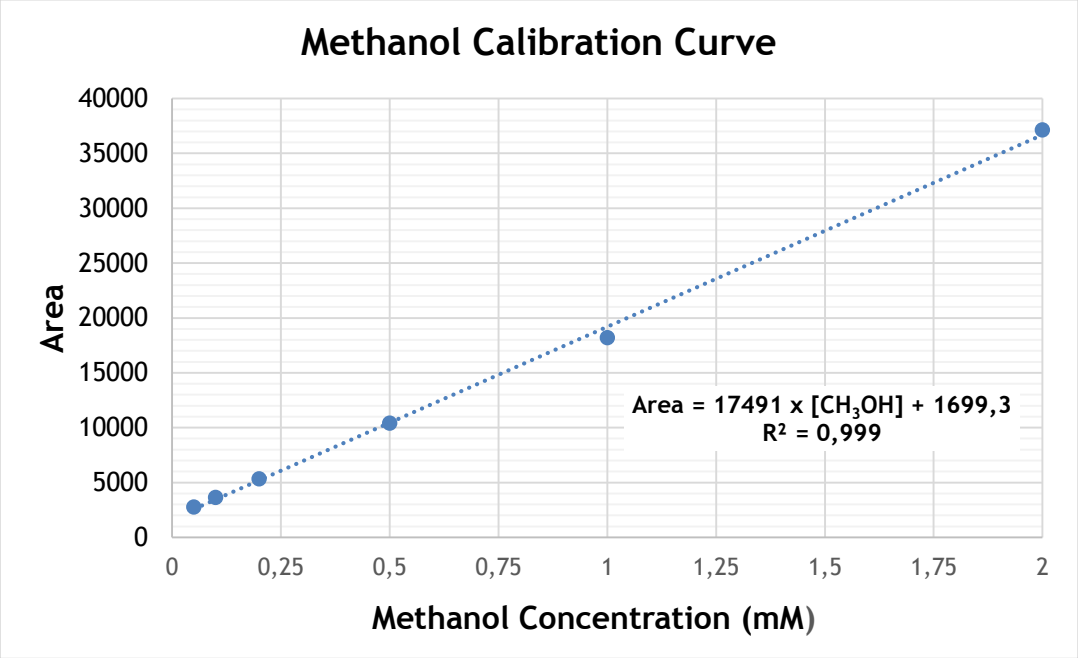

Figure 28 – Methanol Calibration Curve

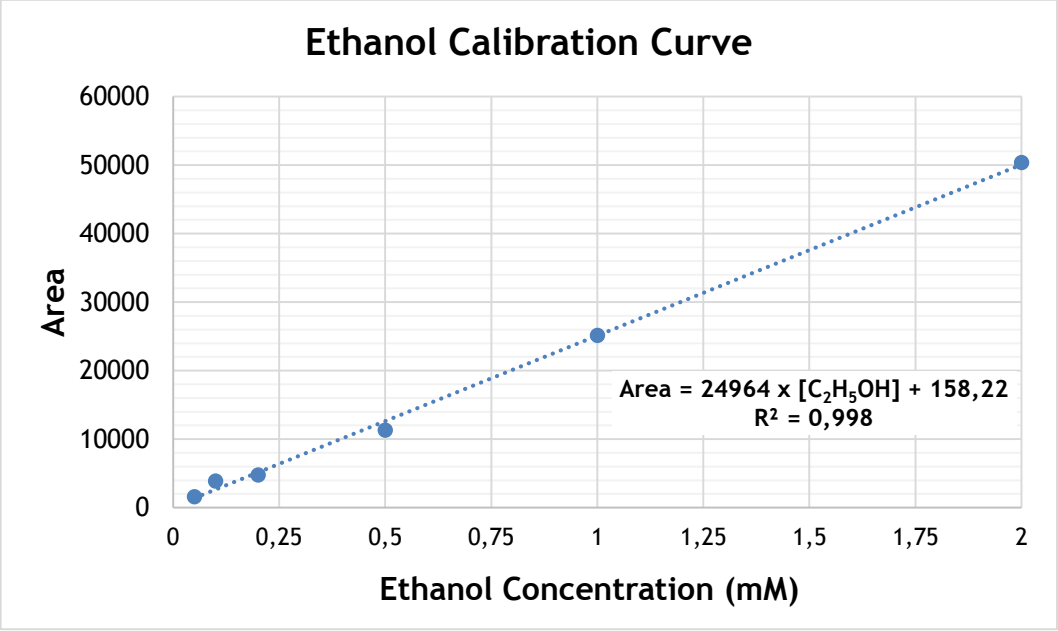

Figure 29 – Ethanol Calibration Curve